GROUP VELOCITY DISPERSION MANAGEMENT IN TERAHERTZ WIRELESS COMMUNICATION CHANNELS

By

KARL STRECKER

Bachelor of Science in Electrical Engineering

Oklahoma State University

Stillwater, Oklahoma

2018

Submitted to the Faculty of the
Graduate College of the
Oklahoma State University
in partial fulfillment of
the requirements for
the Degree of
MASTER OF SCIENCE
May, 2020

GROUP VELOCITY DISPERSION MANAGEMENT IN TERAHERTZ WIRELESS COMMUNICATION CHANNELS

Thesis Approved:

Dr. John O'Hara

Thesis Adviser

Dr. Weili Zhang

Dr. James West

Name: KARL L. STRECKER

Date of Degree: MAY, 2020

Title of Study: GROUP VELOCITY DISPERSION MANAGEMENT IN TERAHERTZ WIRELESS COMMUNICATION CHANNELS

Major Field: ELECTRICAL ENGINEERING

Abstract: High-fidelity models of the atmosphere from 0.1 to 1 THz based on spectroscopic databases are used to examine the effect of group velocity dispersion on ultra-wideband THz links. Previous spectroscopic characterization of THz channels predicts a limit on bit rate caused by group velocity dispersion, but spectroscopic characterizations are limited in their ability to account for important communication link parameters such as signal to noise ratio and maximum allowable symbol error rate. Realistic, statistical studies of the effect of atmospheric dispersion over the 0.2-0.3 THz wireless channel are presented, which account for these parameters and illustrate how future ultra-wideband THz communication systems may not be limited by loss, but by inter-symbol interference, stemming from group velocity dispersion.
A method to compensate atmospheric group velocity dispersion of terahertz pulses is also reported and demonstrated. In ultra-wideband terahertz wireless channels, the atmosphere reshapes terahertz pulses via group velocity dispersion, a result of the frequency-dependent refractivity of air. Without correction, this can significantly degrade the achievable data transmission rate. A method for compensating the atmospheric dispersion of terahertz pulses using a cohort of stratified media reflectors is presented. Using this method, group velocity dispersion in the 0.2-0.3 THz channel under common atmospheric conditions was compensated. Based on analytic and numerical simulations, the method can exhibit an in-band power efficiency of greater than 98% and dispersion compensation up to 99% of ideal. Design simulations were validated by experimental measurements.

TABLE OF CONTENTS

LIST OF TABLES

Table Page

LIST OF FIGURES

Figure Page

Figure Page

CHAPTER I

INTRODUCTION

The demand for high-bandwidth wireless connectivity has increased greatly over the last decade [1] [2] [3]. New technologies and concepts such as machine-to-machine communication, the Internet of Things, and virtual reality are poised to continue this trend by generating massive amounts of data [4] [5], all of which will need to be transported between agents, often wirelessly [6]. Fifth-generation (5G) wireless systems are emerging, and their advent will surely increase global wireless capacity. However, predictions of global data consumption based on current trends indicate that data rates higher than 5G systems can support will be necessary to handle the communication needs of the near future [6] [7].

Terahertz (THz) links – often referred to as 'millimeter-wave' links – are a popular candidate for future high-bandwidth wireless communications, either to augment or succeed 5G systems [5] [7]. The THz frequencies, in this thesis defined as those lying between 0.1 and 10 THz, are largely unlicensed and offer massive bandwidths of several tens of GHz [8], in contrast to existing microwave systems whose heavily crowded channels have bandwidths of at most only a few tens of MHz. This makes THz communication technology capable of handling vast amounts of data. Much work has already been done to develop both short-range (indoor and kiosk-type) and long-range (outdoor) THz links [9] [10] [11].

Some outdoor THz links have spanned distances in excess of 20km [12], which gives hope that wireless THz links may one day provide a substitute for trenched fiber, if not as a complete replacement, then at least as a low-cost alternative. While wireless THz systems will never reach the colossal bandwidths supported by modern fiber optics, they do have several distinct advantages over their optical counterparts. Firstly, wireless THz systems can be set up and made operational much faster than an optical cable can be trenched. This makes THz links attractive for situations that require rapid set-up with minimal existing infrastructure, such as disaster recovery, emergency connectivity after the loss of a fiber link, or semi-permanent communication links in a wartime environment. Photonic THz technology is especially appealing in disaster recovery applications due to its ability to seamlessly integrate with existing fiber optic communication systems [13]. Secondly, THz links provide high-bandwidth connectivity in situations where laying fiber optic line may not be economically viable, in situations such as serving high-bandwidth internet to rural communities and remote scientific sites, over rugged or waterlogged terrain [14], or in applications where a physical cable is impossible to realize or prone to breakage (for example, in a link from earth to a geostationary satellite).

Of course, THz links are no magic bullet – they come with their own set of challenges and drawbacks. One such drawback is that THz radiation must propagate through the dynamic (and non-engineerable) atmosphere, rather than through a static, shielded fiber that can be manufactured to provide optimal channel characteristics. To be specific, the atmosphere inhibits point-to-point THz links via two primary mechanisms: absorption and group velocity dispersion (GVD). Of these two, absorption has been the most studied by far, and the interested reader is referred to the literature [15] [16] [17] [18]. GVD, on the other hand, has been only sparsely studied, [19] [20] though it will be discussed at length in the sections to follow. The prevailing assumption in the literature seems to be that absorption is by far the dominant mechanism impacting THz propagation, thus GVD can be assumed inconsequential and neglected from THz

link budget analyses entirely [21]. However, this thesis will demonstrate that this assumption is invalid. In many relevant cases GVD, not absorption, is the limiting factor for wireless THz communication links.

CHAPTER II

REVIEW OF LITERATURE

Developing accurate channel models is a critical step toward the development of robust THz communication links. Because the characteristics of the atmosphere play such a huge role in determining how successfully data is transmitted over a wireless channel, extensive work has already been done to characterize and model the atmosphere at THz frequencies, with the ultimate goal of enabling us to predict – and then proactively compensate – the effects of the atmosphere on THz data transmission. The purpose of this chapter is to provide an overview of these efforts and show how they lay the foundation for the work described in the remainder of this thesis.

In 1945, Van-Vleck and Weisskopf integrated the work of Lorentz and Debye into a unified theory of the shape of collision-broadened absorption lines [22]. This laid the theoretical groundwork for high-accuracy predictions of atmospheric attenuation and refractivity, given that sufficient information regarding the location and strength of atmospheric molecular species absorption lines is known [23]. Work to spectroscopically analyze the atmospheric composition and molecular response at THz frequencies is publicly available in the JPL [24] and HITRAN [25] databases.

Further refinements to the database-based atmospheric models – particularly in regards to modeling continuum absorption at THz frequencies – were subsequently made, especially as the development of terahertz time-domain spectroscopy (THz-TDS) in 1997 allowed highly precise, phase-coherent measurements of atmospheric absorption spectra [26] [27] [28]. The introduction of Molecular Response Theory (MRT), which performs a frequency dependent fractional sum of van Vleck-Weisskopf and full Lorentz absorption models, brought theoretical predictions into very good agreement with empirically measured results [29]. This enabled the frequency-domain response of the atmosphere to be modeled with high fidelity over the proposed THz communication bands [14], paving the way for highly accurate numerical predictions of atmospheric effects on THz signal propagation.

Further research in the area of ultra-wideband pulse propagation [20] showed and experimentally verified that the atmosphere not only attenuates, but also reshapes, ultra-wideband pulses through both spectral absorption and group velocity dispersion (GVD) [30] [31] [32]. In the context of communication links, GVD results in temporal broadening of transmitted symbols, and sufficiently severe GVD may cause neighboring communication symbols to merge, making them irresolvable in an undesirable phenomena known as intersymbol interference (ISI).

Of particular interest to this thesis is the work of Mandehgar *et al*. in 2014, in which they observed that in some cases GVD – not absorption – becomes the limiting factor in the maximum bandwidth-distance product a THz wireless link may have [30]. Their paper makes predictions based on impulse broadening about what this limit will be for various THz channels, but no calculations are provided for more spectrally efficient modulations such as QPSK. As Mandehgar *et al*. themselves state, their work also does not account for the effects of signal-to-noise ratio (SNR) or maximum allowable symbol error rate (SER) on achievable bitrate, which need to be considered to get a more accurate picture of how the proposed dispersion limit will behave. This is the closest any known published work (at the time of this writing) has come to a

comprehensive analysis of atmospheric effects on THz data transmission. While non-statistical methods based on impulse broadening are useful in demonstrating the effects of dispersion, the lack of simulations using modulated data streams, and accounting for SER and SNR in addition to both attenuation and GVD, represents a critical knowledge gap to be filled. As stated by Ma *et al*. in their 2018 channel characterization, the evaluation of THz wireless links by the transmission of modulated data streams can provide insights into the dynamics of channel performance that spectroscopic characterization alone cannot provide [7].

In the meantime, physical THz communication links have been designed, implemented, and analyzed by several research teams, many with the express intention of channel analysis. For a comprehensive overview of experimental links demonstrated to date, the reader is referred to survey literature such as references [7] [9] [33]. Of particular interest to this thesis, however, are those links operating at high bandwidth-distance products (Gbit-km/s), as these links are most susceptible to dispersion. In the past decade, point-to-point outdoor THz links of increasing length and data rate have been demonstrated. In 2012, a link operating at 140 GHz successfully transmitted data at a rate of 10 Gbit/s over a distance of 1.5 km at a bit error rate of less than 10^{-6} [34], and another 10 Gbit/s link was demonstrated over 5.8 km, which used BPSK modulation and a carrier frequency of 120 GHz [35] [36]. The data rate was pushed even higher in 2015, with the demonstration of a 64 Gbit/s link operating over 0.85 km, utilizing a 240 GHz carrier wave in the broad 250 GHz atmospheric window [37]. The highest bandwidth-distance product for a link reported in the literature (at the time of this writing) was set just a few years later in 2017, spanning 21 km and achieving 5 Gbit/s using 16-QAM modulation at 140 GHz [38].

The attentive reader may notice that atmospheric attenuation is given much consideration in these articles, yet discussion regarding atmospheric dispersion is conspicuously absent. However, this is readily explained. In the work of Mandehgar *et al*. [30], in which dispersion in THz wireless communication channels is clearly shown, the bandwidth-distance products of the links

considered is much higher than that of the links experimentally demonstrated. While the recent advances in long-distance THz point-to-point links is impressive, the technology is yet in the early stages of development and has not yet reached the point where distance-bit rate products are high enough to observe the impact of atmospheric dispersion. However, if the rapid advances in THz technology continue, it is likely that point will be reached within the next few decades.

To summarize, extensive work has already been done to characterize the atmosphere at THz frequencies, resulting in a wealth of technical data on atmospheric properties. These studies of the atmosphere are extremely valuable, however, the vast majority of them have been spectroscopic in nature, rather than using a modulated data stream to measure or simulate the actual transmission of data through the channel. Spectroscopic characterization is fundamental and necessary, but it has limited ability to quantifiably predict how changing atmospheric conditions will impact the channel limit on SER. On the other hand, physical THz links implemented to date – which necessarily experience all atmospheric effects – are subject to technological limitations, and cannot explore certain high-bandwidth link configurations simply because the underlying technology is still in the early stages of development. This prevents the observation and analysis of certain phenomena, data corruption due to GVD at high bandwidth-distance products being one example. This work explores a “blind spot” in THz link development, and builds on previous work by leveraging high-fidelity models of the atmosphere to simulate the transmission of modulated data over the millimeter-wave channel centered at 250 GHz, and draw fundamental and highly practical conclusions about the impact of group velocity dispersion (GVD) on THz data transmission through the atmosphere at high bandwidths.

CHAPTER III

ATMOSPHERIC MODELING

SECTION I – METHODOLOGY

The atmosphere was modeled using the methodology of Mandehgar *et al*. [31], using the HITRAN database to provide information regarding the frequency, resonance strength, and broadening factor of each molecular resonance for both water vapor and oxygen. Only the data for resonances near enough and strong enough to influence the frequency band of interest was extracted. This includes resonances up to about 5 THz, whose extremely strong lines have wings that extend into the 0-1 THz regime with significant strength. For each resonance, the extracted parameters of frequency, resonance strength, and broadening factor were used to calculate the collision-broadened line shape in accordance with MRT. The shape of each broadened line depends heavily on the temperature, pressure, and vapor density of the atmosphere, which necessitates recomputing each linewidth whenever one of these parameters is changed. After the linewidth of each resonance has been computed, they are summed over the frequency bands of interest, resulting in the frequency-dependent transfer function of the atmosphere, which accounts for the actions of both absorption and dispersion on propagating radiation. Following this procedure closely replicated the work of Mandehgar *et al.* in their 2013 paper; plots of the attenuation and phase shift produced by the atmospheric model are shown in Figure 1, and should be compared to the absorption and refractivity of the atmosphere as computed by Mandehgar *et al* [14] .

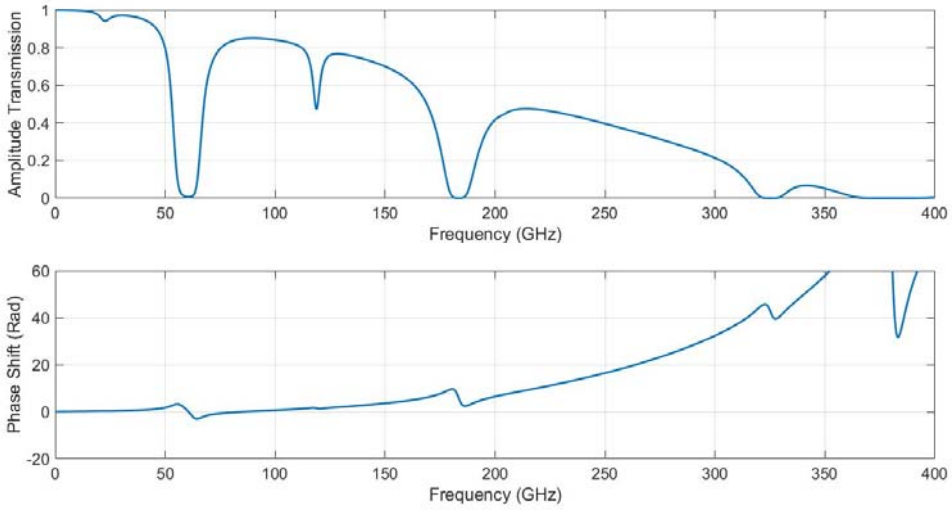

Figure 1 - Atmospheric absorption and phase shift for a 2 km path length with a water vapor density of ρ_{wv} = 10 g/m^3 at 20°C. Compare to Figure 2 in Mandehgar 2013 [14].

Once the frequency-dependent phase $\varphi(\omega)$ and attenuation $\alpha(\omega)$ are known for a specific atmospheric channel (as in Figure 1 or Figure 2), the effects of the modeled atmosphere on an arbitrary terahertz signal can be found by a frequency-domain multiplication of the complex atmospheric spectrum and the complex signal spectrum, $E_{out}(\omega) = E_{in}(\omega)e^{j\varphi(\omega)}e^{-\alpha(\omega)}$, where $E_{in}(\omega)$ is the spectrum of the electric field of the transmitted THz signal. The output signal spectrum $E_{out}(\omega)$ may be converted to time-domain by an inverse Fourier transform (IFFT). This procedure fully accounts for the atmosphere's action on both amplitude and phase, including higher order dispersion, and was used throughout the extent of this research effort to model the atmosphere to a high degree of accuracy. Readers are referred to the work of Yang, Mandehgar, and Grischkowsky [20] for the mathematical development of atmospheric transfer functions.

SECTION II – RESULTS

In our discussion of the results of atmospheric modeling – and in our discussion of dispersion in general – it is necessary to understand the terminology used. Of particular importance are the

terms “group delay,” “group delay dispersion,” “group velocity,” and “group velocity dispersion” (or GVD), as well as the relationship between them.

Group delay possesses units of time, and is defined as the rate of change of spectral phase with respect to angular frequency, $t_g(\omega) = \frac{d}{d\omega}\varphi(\omega)$ [39]. Group delay may be intuitively understood as the propagation delay experienced by a narrowband pulse of frequency ω as it travels through the medium. In a dispersive medium such as the atmosphere, group delay varies with frequency, so a broadband pulse (which contains many frequency components) will temporally disperse as its component frequencies travel at different velocities. Group delay most commonly increases with frequency, producing normal dispersion; If it decreases with frequency, this is known as anomalous dispersion.

Group delay dispersion is defined as the rate of change of group delay with respect to angular frequency [40], or the second derivative of spectral phase with respect to angular frequency: $d_g(\omega) = \frac{d^2}{d\omega^2}\varphi(\omega) = \frac{d}{d\omega}t_g(\omega)$. For this reason, group delay dispersion is sometimes referred to as “second order dispersion,” and it is a measure of how dispersive a media is. Group delay dispersion possesses units of time squared.

Both group delay and group delay dispersion depend on the propagation path length. Group velocity, on the other hand, does not: it is computed as the inverse of group delay per unit distance, $v_g = \left(\frac{t_g}{L}\right)^{-1}$, and is the speed at which a narrowband pulse will propagate through the material. Fundamentally, group velocity measures the same quantity at group delay, but normalized to unit length. Similarly, GVD is group delay dispersion normalized to unit distance.

Even though this thesis is concerned with the management of GVD, most of the plots and discussions of dispersion will be put in terms of group delay, or occasionally group delay dispersion. In our analysis of discrete, monolithic THz dispersion compensating devices, this will

be the most natural way to discuss dispersive effects, as normalizing the behavior of discrete devices to unit length is unhelpful and can be misleading (see chapters V and VI). With that in mind, let us now discuss the characteristics of the atmosphere over the 0.1 – 1 THz band.

Figure 2 shows the characteristics of the atmosphere up to 400 GHz, normalized to propagation over one kilometer. From the plot, it can be seen that neither attenuation nor group delay are constant, either as a function of frequency or vapor density. This indicates that the atmosphere will cause temporal dispersion, and that such dispersion will increase and decrease with changing atmospheric conditions.

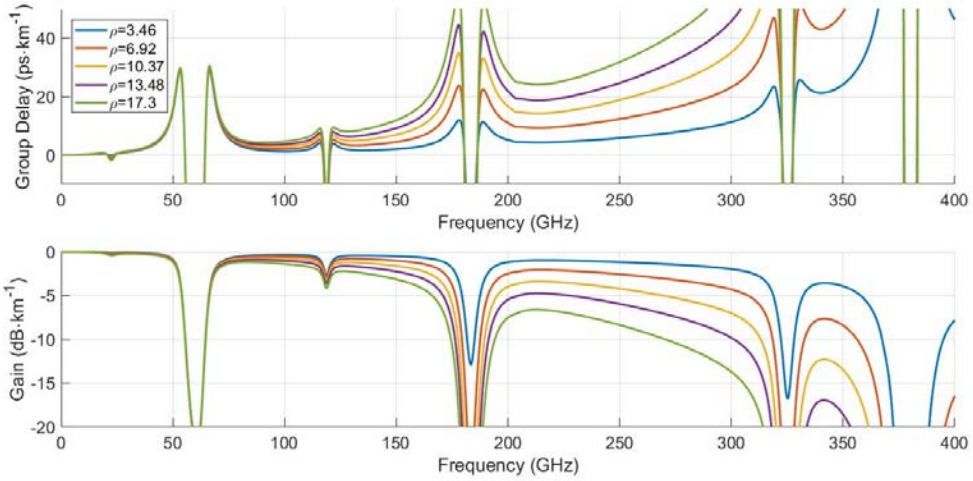

Figure 2 - Atmospheric modeling result of the long-distance THz communications bands, for frequencies up to 400 GHz and vapor densities of 3.46, 6.92, 10.37, 13.48, and 17.3 g/m^3. Temperature = 20 °C.

While there are several atmospheric windows lying below 1 THz, only some are suitable for long-distance communication, due to increasingly strong attenuation by atmospheric water vapor at higher frequencies. For this reason, and for the sake of brevity, we will focus our analysis on the atmospheric window centered at 250 GHz. The 250 GHz channel lies between the 183 GHz and 325 GHz water vapor absorption lines [14], possesses the highest contiguous bandwidth of any THz channel, and suffers from relatively little dispersion and attenuation compared to most other

THz windows [31]. This makes it an excellent case study for the analysis of long-distance, high data rate THz links.

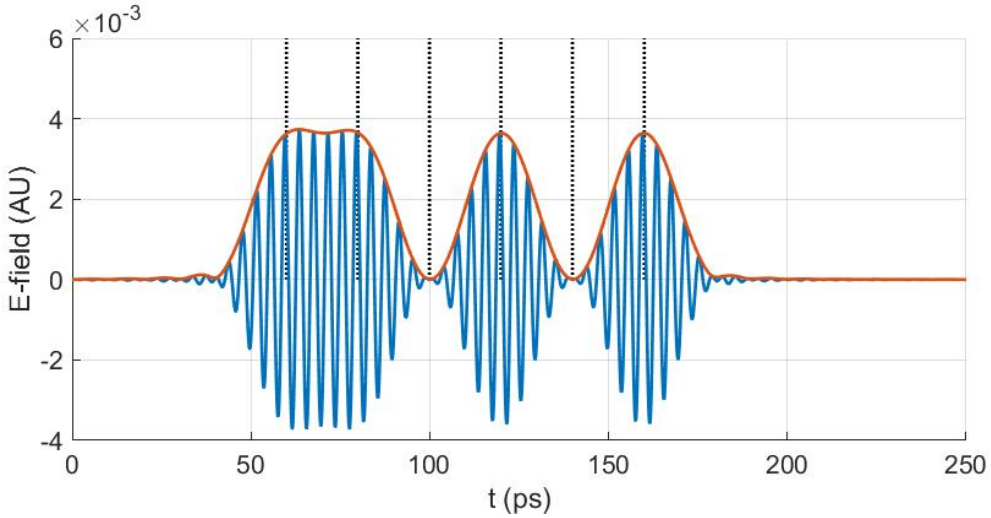

Figure 3 - Ideal impulse-encoded bit sequence 11010 before propagation through the atmosphere. The link is centered at 250 GHz, possesses a full width at half maximum bandwidth of 50 GHz, and exhibits excellent bit resolution. The dashed vertical lines represent the points at which the signal is sampled.

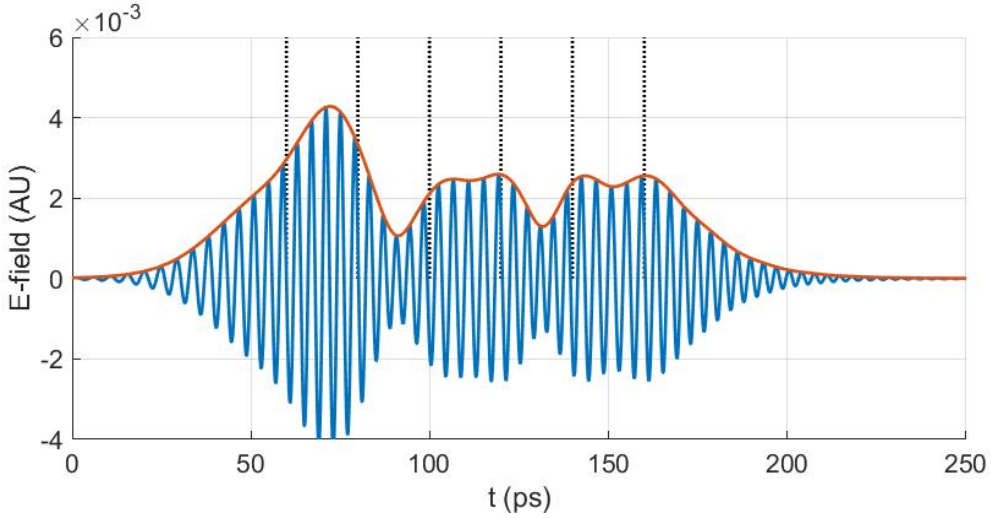

Figure 4 - Dispersed impulse-encoded bit sequence 11010 after propagating 4 km through the atmosphere at ρ_{wv} =10.37 g/m^3 (60% relative humidity), T=20°C. The pulse shapes are heavily distorted by GVD, and have merged together which inhibits bit resolution. The dashed vertical lines represent the points at which the signal is sampled.

Figure 3 and Figure 4 present a simple illustration of how the atmosphere reshapes broadband THz data signals through GVD. In the plots, the 6-bit sequence “110101” is encoded as a

sequence of THz pulses, which are centered at 250 GHz, and possess a full width at half maximum (FWHM) bandwidth of 50 GHz. Figure 3 shows the ideal bit sequence as it would be transmitted, and Figure 4 shows the same bit sequence after propagating 4 km through the atmosphere described in the figure caption. The waveform of Figure 4 has been amplified by a factor of 6.97 to offset atmospheric losses and facilitate comparison with Figure 3. It is evident from Figure 4 that the atmospheric phase shift over the 250 GHz band is sufficient to cause ISI between neighboring symbols and corrupt the data stream, even though the atmospheric loss of 8.43 dB is easily overcome and no noise was added to the signal. This demonstrates that in some cases GVD, and not atmospheric attenuation, will be the limiting factor on the performance of at THz wireless link.

CHAPTER IV

NUMERICAL LINK SIMULATION

SECTION I – METHODOLOGY

The atmospheric models were used to numerically simulate the transmission of pseudo-random digital data over a broadband terahertz link in order to predict the impact of GVD on SER under various link configurations and atmospheric conditions. The pseudo-random data sequences were generated in frames of *N* symbols, and the serial transmission of each frame through the atmosphere was simulated. By comparing the data in each frame before and after transmission through the modeled atmosphere, the number of symbol errors can be counted. By repeating this process many times, a statistical SER for the link is predicted. The simulation process is described in greater detail in the following paragraphs. The numerical simulations were performed using MATLAB®.

First, the link parameters of transmission distance, symbol rate, and center frequency were chosen, and the atmospheric properties of water vapor density and temperature defined. This set both the sampling frequency and maximum allowable bandwidth, and allowed the atmospheric model to be generated with proper frequency resolution.

Data frames were then serially generated and transmitted through the atmosphere. Each frame contained *N* symbols of pseudo-random data, or $\log_2(M) \times N$ bits, where *M* is the modulation

order of the link. *M* may be any power of 2, but in the simulations described in this thesis, it may be assumed that $M = 4$, $N = 500$, and QPSK (4-QAM) modulation was used. Each symbol may take integer values in the range 0 to $M–1$, and these integer values were mapped into complex-valued numbers in IQ space, according to Table 1. In Table 1, binary data is mapped to symbol number using Gray coding, which favorably alters the relationship between SER and bit-error rate [41]. However, in this work link performance will be discussed in terms of SER directly, so the particular encoding used is irrelevant to the results of the simulation.

SYMBOL	BINARY DATA	COMPLEX REPRESENTATION
0	00	$e^{j\pi/4}$
1	01	$e^{j3\pi/4}$
2	10	$e^{j7\pi/4}$
3	11	$e^{j5\pi/4}$

Table 1 - Relationship between symbol name, binary, and IQ (complex) representations. The binary data is mapped to symbol number using Gray coding.

The frame was then converted from a sequence of discrete complex-valued symbols to a continuous time-domain signal by up-sampling the symbol sequence at 1 THz. In accordance with the Nyquist criterion, this allowed frequency components up to 500GHz to be resolved without aliasing [42]. This was sufficient for our simulation process, as the strong water vapor attenuation line at 325 GHz placed an upper bound on the maximum frequency component that could be contained in the signal. This up-sampled waveform was pulse shaped with a square root raised cosine filter, implemented as a MATLAB® system object, with a roll-off factor of 0.5 and a symbol span of 6 symbols. This filter eliminated intersymbol interference (under dispersionless conditions) while confining the signal spectrum to a finite bandwidth contained within the

atmospheric window. At this point in the process, the frame of data had been converted from a discrete symbol sequence to a continuous time-domain baseband waveform.

This baseband signal was split into its real and complex components, which were mixed with the in-phase and quadrature components respectively of a carrier wave, $e^{-j2\pi f_c t}$, where f_c is the center frequency. This shifted the baseband signal up in frequency, centering it at f_c. The choice of f_c determines in which atmospheric window the signal will propagate. For long-distance communication with minimal dispersion, f_c should be chosen to lie in the middle of one of the broad atmospheric windows. In the simulations discussed here, f_c = 250 GHz.

The time-domain signal, now modulated onto a carrier wave, was converted to a complex amplitude spectrum in the frequency domain by fast Fourier transform (FFT), an implementation of the Fourier transform $E_{in}(\omega) = \int_{-\infty}^{\infty} E_{in}(t)e^{-j\omega t}\, dt$ for discrete (sampled) data. The propagation of the signal through the atmosphere was simulated by frequency-domain multiplication of the signal's amplitude spectrum with the complex transfer function of the atmosphere, $E_{out}(\omega) = E_{in}(\omega)e^{j\varphi(\omega)}e^{-\alpha(\omega)}$. The product was converted back to time domain by inverse fast Fourier transform (IFFT), an algorithm which implements the inverse Fourier transform function $E_{out}(t) = \frac{1}{2\pi}\int_{-\infty}^{\infty} E_{out}(\omega)e^{j\omega t}\, d\omega$. The resulting complex time-domain waveform was a time-shifted, attenuated, and dispersed version of the input, valid in accordance with linear dispersion theory [20].

However, to quantify the effect of dispersion on a signal, it must be demodulated and returned to a discrete sequence of symbols. In general, noise must also be injected at this point, because a noiseless link is unaffected by atmospheric attenuation, so white Gaussian noise was added to the signal at a known SNR, or at a constant level (noise floor), depending on the simulation being run. Demodulation was performed by mixing the post-atmosphere signal with a phase-synchronized local oscillator (LO) of unit power and frequency f_c, simulating a homodyne

detection scheme. In a physical communication system, the SNR of the receiver would in general depend on the power of the LO, which may be increased to overcome thermal noise in the receiver [43]. However, hardware details such as LO power and receiver noise characteristics are irrelevant to the results of the simulations presented here as we defined the SNR at the receiver directly. Doing so abstracts away the implementation details, making the results applicable to arbitrary THz communication systems.

Mixing the signal with the LO returned the signal to baseband, and the frequency-doubled component centered at $2f_c$ was removed with a matched square root raised cosine filter. The filtered signal was time-shifted relative to the input due to finite propagation velocity through the atmosphere, and this time-shift was removed by calculating the group delay at frequency f_c as $t_g(f_c) = \frac{d}{d\omega}\varphi(2\pi f_c)$ and shifting the received signal backward in time by $t_g(f_c)$. This constant time shift did not affect the group delay dispersion, but it did ensure that the received signal was sampled at the ideal locations. After time-shifting, the signal was then downsampled at a rate of one sample per symbol. The sampled data was fed to a decision logic block, which for a noiseless, dispersionless link would perfectly recover the transmitted symbols, as depicted in Figure 5. However, in the presence of both dispersion and reduced SNR due to attenuation, some of the decoded symbols may be in error, as shown in Figure 6. These errors are identified by comparing the transmitted and received data frames, and the number of errors was summed.

By repeating this procedure many times, the SER of the link was predicted as $SER = N_e/N_T$, where N_E is the total number of errors observed, and N_T is the total number of symbols transmitted. By iterating the entire simulation process over parameters such as symbol rate (bandwidth), SNR, or atmospheric water vapor density, the relationship between SER and various link parameters was explored.

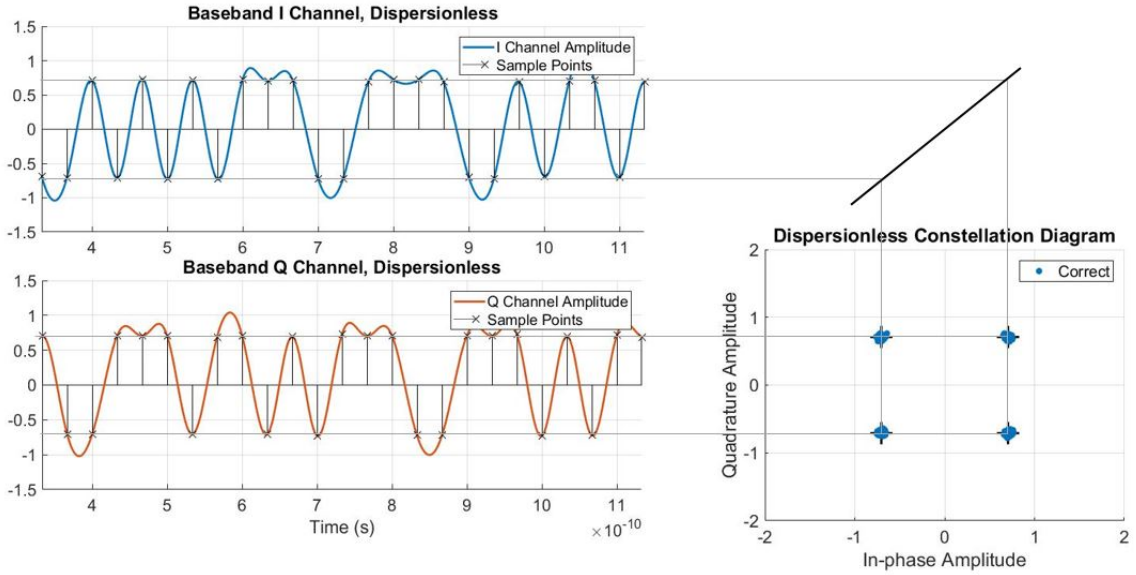

Figure 5 - In-phase and quadrature components of a noiseless, dispersionless signal after downshifting and filtering at the receiver. When sampled at the ideal locations as shown, the transmitted symbols are recovered with high certainty, as indicated by the tight symbol grouping on the constellation diagram. The link shown has a 30 GHz FWHM bandwidth, and a center frequency of 250 GHz.

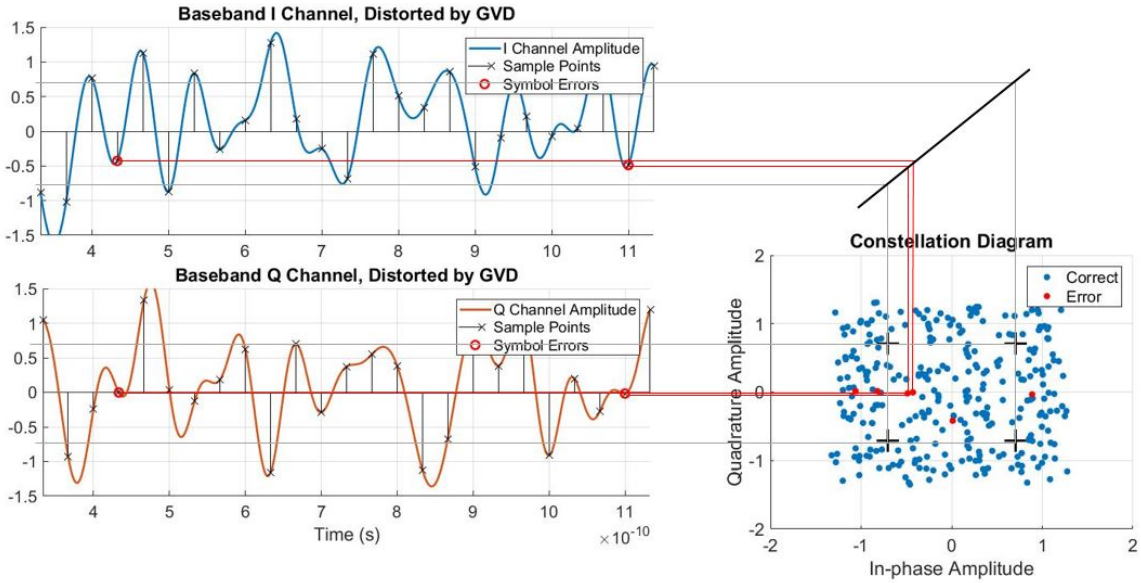

Figure 6 - In-phase and quadrature components of a noiseless but heavily dispersed signal after downshifting and filtering at the receiver. In this figure, the symbols transmitted are identical to those in Figure 5, but have propagated 4 km through the atmosphere at ρ_{wv} =10.37 g/m^3 (60% relative humidity) and T=20°C. ISI caused by GVD has distorted the waveforms so badly that, even when sampled at the ideal locations, several of the symbols are in error.

SECTION II – RESULTS

In the simulations of modulated data transmission through the atmosphere, there are in general four quantities of interest whose relationships this section will explain. These four parameters are the distance spanned by the THz link, the bandwidth used by the link, the SNR at the receiver, and the SER at the receiver. It is important here to note that link bandwidth is related to data rate by the modulation type used in the link, as some modulation schemes are more spectrum-efficient than others. Because a single modulation type (QPSK) is assumed in all following discussion, the parameter of signal bandwidth will be frequently expressed as symbol rate. Throughout this section, symbol rates will be given in terms of billions of symbols per second, denoted G/s. Because each symbol carries two bits of information, the bit rate (given in units of Gbit/s) will be twice the symbol rate for any given link.

The four link parameters of interest are related through the two atmospheric effects of absorption and chromatic dispersion (effects on the amplitude and phase of the THz signal, respectively). It is important to note that frequency-dependent absorption is inseparable from frequency-dependent phase effects due to Kramers-Kronig relations, however, uniform (frequency-independent) reductions in signal power do not affect the frequency-dependent phase of the wave, and vice versa [44]. By assuming that reductions in SNR are due to uniform attenuation of the signal, the effects of atmospheric absorption on SER can be separated from those of dispersion by defining the SNR at the receiver directly, which makes interpreting the results of the simulation simpler.

Before examining the results of the simulation, however, it is prudent to clarify how absorption and dispersion relate the four link parameters. First, the distance of the link will directly affect both attenuation and dispersion; longer links experience both higher dispersion and attenuation than shorter links. The signal bandwidth affects only dispersion (assuming frequency-independent

absorption), and a high-bandwidth signal will suffer more severe dispersion than a narrowband signal. The SNR at the receiver is affected only by absorption, which reduces the signal power. Finally, SER is the final standard by which the communication link is measured: the SER must not be so high as to prevent the reliable transmission of data. SER is affected by both dispersion (which causes ISI) and attenuation (which decreases SNR), and – perhaps surprisingly – the simulation results show that neither effect is unequivocally dominant: both attenuation and dispersion may be the atmospheric mechanism that determines the lower bound on SER.

Let us consider the "classical" (dispersionless) case of a narrowband wireless communication link. As transmission distance increases, the SNR of the signal is degraded due to atmospheric attenuation, however, signal bandwidth is irrelevant so long as the signal lies within the semi-constant absorption window in the atmosphere. This is a valid assumption for narrowband signals. For dispersionless links the relationship between SER and SNR is well-understood, and closed-form theoretical equations relating the two have been developed. For a QPSK link, this formula is $SER = \text{erf}\left(\sqrt[2]{\frac{SNR}{2}}\right) - \frac{1}{4}\left[\text{erf}\left(\sqrt[2]{\frac{SNR}{2}}\right)\right]^2$, where SNR is the signal-to-noise ratio of the link expressed as a linear value (not in dB), and the error function $\text{erf}(x) = \frac{2}{\sqrt{\pi}}\int_0^x e^{-t^2}dt$ [45]. The relationship between SER and SNR can be seen plotted in Figure 7. This plot is frequently called a waterfall plot, and it represents the limit placed on SER by atmospheric attenuation alone. On the other hand, we can examine the effects of dispersion without attenuation by performing the simulation process described in chapter 3, but injecting no noise (that is, setting the SNR at the receiver to be infinite) and sweeping the distance parameter. Physically, this would correspond to having an arbitrarily powerful transmitter capable of overcoming any atmospheric losses. By eliminating the effects of attenuation, increasing the distance parameter of the simulation will increase dispersion only. The results of these simulations for various symbol rates are shown in Figure 8.

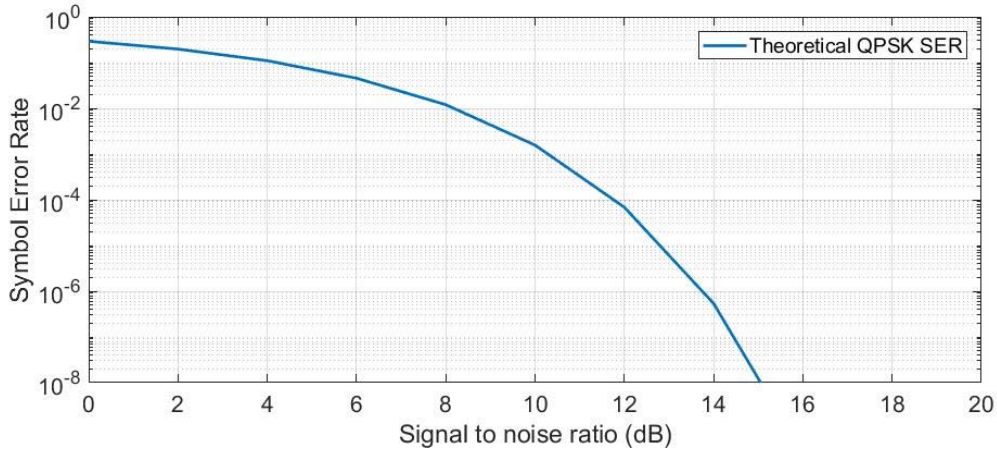

Figure 7 - Relationship between SNR and SER for a dispersionless QPSK link. Noise is assumed to be white Gaussian noise.

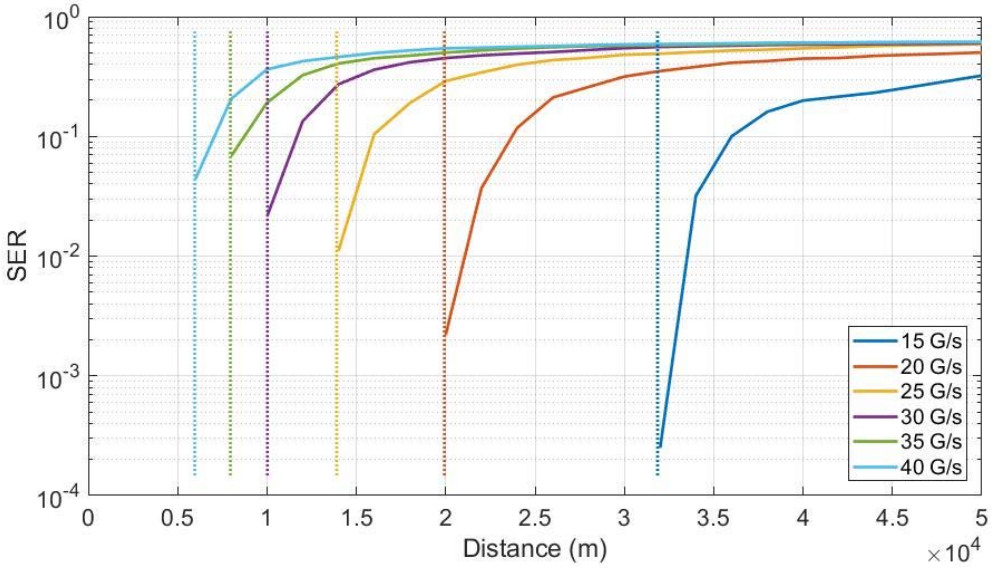

Figure 8 - Symbol error rate versus distance for various symbol rates, with infinite SNR. Atmospheric conditions are ρ_{wv} =10.37 g/m^3 (60% relative humidity), T=20°C. Symbol rates are in gigasymbols per second, and modulation type is QPSK. Dispersion limits are indicated by dotted vertical lines.

The results shown in Figure 8 are quite significant; they reveal a "dispersion limit" on the range of THz wireless communication, which is shown by the sudden jump in SER from error-free operation to values exceeding 1 in 10 over less than a 5 kilometer increase in distance. These "dispersion limits" are marked on the graph by vertical dotted lines, and error-free operation may

only be experienced at distances below the dispersion limit. The implication is that no matter how powerful a transmitter is used, or how sensitive a receiver is developed, there exists a finite range a THz signal of a given bandwidth can propagate before ISI caused by uncompensated GVD renders the link inoperable. For example, as seen in Figure 8, a 20 G/s (40 Gbit/s QPSK) link cannot extend farther than 20 km while maintaining a SER below 10^{-3}, while a 30 G/s (60 Gbit/s) link is restricted to less than 10 km range for the same SER, for the atmospheric conditions detailed in the figure caption. It should be noted that increasing the vapor density of the atmosphere has a very similar effect on the dispersion limit as increasing the distance of the link. This is rather intuitive, as both actions serve to increase the total amount of water vapor and molecular oxygen that interact with the THz beam.

It is also evident from Figure 8 that reductions in bandwidth greatly increase the dispersion limit, as illustrated by the increasing distance between the dispersion limits (vertical dashed lines) with decreasing symbol rate. In fact, a 10 G/s (20 Gbit/s) link has a dispersion limit beyond 50 km, and is not visible in Figure 8. Dispersion limits of this range and greater can be neglected for single links, because earth-curvature effects will limit the range of a line-of-sight link before the dispersion limit is reached. Thus, the assumption that atmospheric absorption is the limiting effect on THz data transmission range is valid for low symbol rates, but not for high ones.

In reality, it is unrealistic to assume that atmospheric attenuation plays no role in limiting the maximum transmission distance of a THz wireless link. It is instructive to see the effect that decreasing SNR at the receiver due to attenuation has on the dispersion limit of a link. Rather than considering the complexities of how distance, transmitter power, receiver sensitivity, and a host of other factors combine to determine SNR at the receiver, we will abstract away the details of the link implementation by defining the SNR at the receiver directly, again assuming an arbitrarily powerful transmitter is adjusted to produce the desired SNR at the receiver. The results

of the simulation of data transmission through the atmosphere with noise added are shown in Figure 9, Figure 10, and Figure 11.

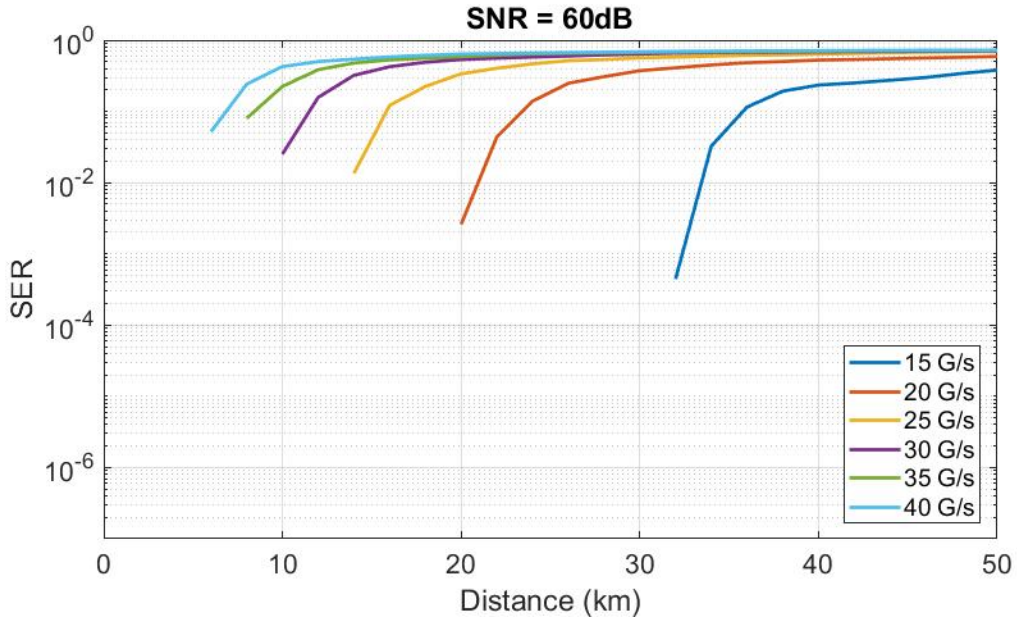

Figure 9 - SER vs distance for SNR = 60dB, through an atmosphere with a water vapor density of ρ_{wv} = 10.37 g/m^3 at 20° C. The SER curves show little difference from those shown in Figure 8, except for a change in figure scaling.

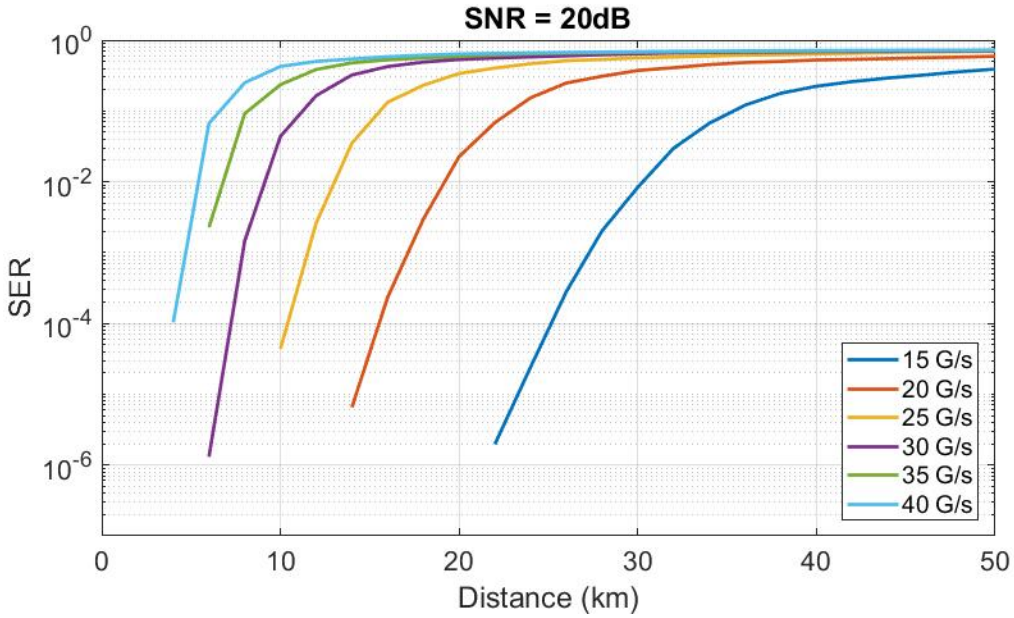

Figure 10 - SER vs distance for SNR = 20dB, through an atmosphere with ρ_{wv} = 10.37 g/m^3 at 20° C. The reduction of SNR from 60 dB in Figure 9 to 20 dB here has lowered the distance at which GVD first begins to cause detectable symbol errors.

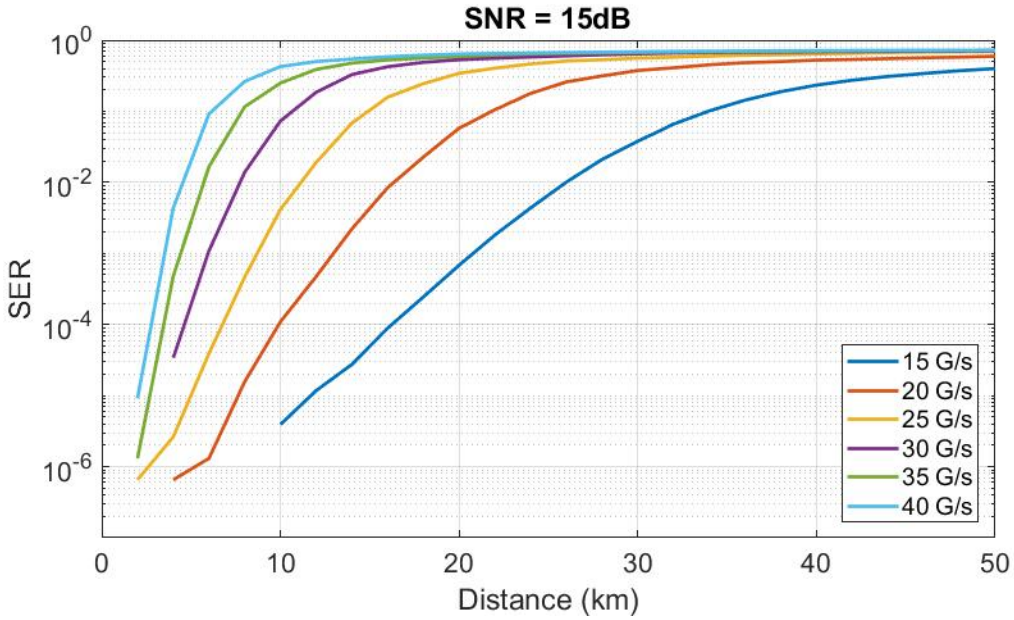

Figure 11 - SER vs distance for SNR = 15dB, through an atmosphere with ρ_{wv} = of 10.37 g/m^3 at 20° C.

From a comparison of Figure 9 with Figure 10 and Figure 11, it can be seen that decreasing the SNR results in a relaxation of the abrupt dispersion limits shown in Figure 8. In Figure 8, the transitions from error-free operation to unacceptable SER are so sharp because dispersion-caused ISI for a noiseless signal is discrete – there is a point at which SER jumps from precisely zero to a finite value as the distortion caused by GVD increases in severity, from almost being enough to produce ISI to actually causing ISI in a particular symbol sequence.

In the absence of noise, and if dispersion is low enough, then no ISI is possible. However, adding noise pushes some dispersion-distorted symbol sequences over the boundary from almost producing a symbol error to actually producing symbol errors, relaxing the transition from error-free to dispersion limited operation. This reduces the range at which dispersion causes a THz link to begin exhibiting symbol errors. Importantly, this means that heavily attenuated signals (that is, signals with low SNR) will suffer an increase in SER due to dispersion, even well below the noise-free dispersion limit.

As an illustration of this, refer to the SER vs distance plot for the 15 G/s (30 Gbit/s) link in Figure 9, Figure 10, and Figure 11. In Figure 9, the SNR is high (60 dB), and a 30 Gbit/s link spanning 25 km is well below the dispersion limit and enjoys error-free operation. However, in Figure 10, the reduction in SNR to 20dB causes an increase in dispersion-induced errors, and the SER at 25 km is increased to 10^{-4}. Further decreasing the SNR to 15 dB raises the error rate at 25 km to 6.6×10^{-3}, and pushes the range for a SER of 10^{-4} back to 16.25 km.

These plots demonstrate that even at link distances well below the dispersion limit, atmospheric dispersion can still significantly impact the performance of a THz link if the SNR is low. It is especially noteworthy that this effect is most pronounced in lower-bandwidth links. From Figure 8, it might be (incorrectly) assumed that low bandwidth links will never suffer dispersion-induced ISI because of their extremely high dispersion limits. However, Figure 11 shows this is not the

case: the SER of the 15 G/s link is strongly increased by the presence of dispersion when the SNR is low. An extremely high dispersion limit does not necessarily imply an absence of dispersion-induced symbol errors; it simply means that for most distances, increasing the SNR of the link will correspondingly improve the SER.

This relationship is made clearer in Figure 12, which shows SER plotted explicitly against SNR for a 20 G/s link, through the same atmospheric conditions as Figure 8. For a very short path (0 km), dispersion is absent and the simulated SER waterfall plot matches the theoretical prediction. However, as dispersion is increased by extending the link distance, the rate at which increasing the SNR decreases the SER is reduced – though for link distances at or below 19 km, SER may still be lowered by increasing the SNR.

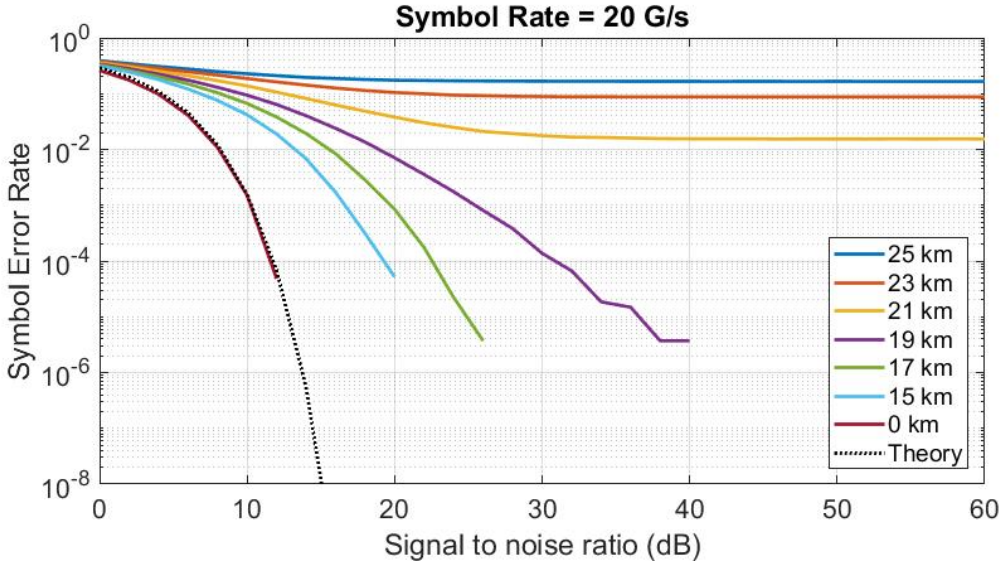

Figure 12 - SER versus SNR for a 20 G/s THz link, through the atmosphere at a water vapor density ρ_{wv} = 10.37 g/m^3 at 20° C, over path lengths of 0, 15, 17, 19, 21, 23, and 25 km. The theoretical waterfall curve for a classical (dispersionless) QPSK link is also shown for reference and overlaps the 0 km data almost exactly.

At or above 21 km however, a significant and fundamental change in behavior is observed: beyond a certain SNR, increasing the SNR of the link yields no improvement in the SER. This is because the link is operating beyond the dispersion limit, and the fundamental limitation on link

performance is no longer determined by SNR. Comparing Figure 12 with Figure 8 reveals that this transition from SNR-limited to dispersion-limited operation occurs at the maximum path length marked on Figure 8 for a 20 G/s link, that is, 20 km. This illustrates the fact that the dispersion limit is not a distance below which dispersion-induced ISI is not observed, but rather a point at which the behavior of the link transitions from absorption-limited to dispersion-limited operation. Beyond the dispersion limit, improvements in link performance may only be obtained through the design and implementation of dispersion-compensating strategies.

CHAPTER V

DESIGN OF DISPERSION COMPENSATOR

SECTION I – METHODOLOGY

As shown in the previous sections, the atmosphere is a dispersive medium. The results of atmospheric modeling show that the group delay of the atmosphere is non-constant with frequency. Though minimized inside the atmospheric windows, nonzero group delay dispersion still causes temporal distortion of THz radiation. The effects of dispersion are the most obvious when considering transform-limited pulses (which dilate visibly in time to produce ISI, see Figure 4 and Figure 16), but any modulation scheme will be impacted by group velocity dispersion, as demonstrated by the simulation of broadband QPSK links in the previous chapter. Regardless of modulation type, nonzero group delay causes the multitude of frequency components contained in a high-bandwidth THz signal to propagate at different velocities through the atmosphere, losing the phase relationship they shared on transmission.

In order to reverse dispersion, the proper phase relation between the signal components must be restored. One way this may be accomplished is by introducing a device into the signal path that has a group delay profile opposite to the atmosphere over the bandwidth of interest. An equivalent statement is that the sum of the GVDs of the inserted device and the atmosphere must be zero. If this is done, then the relative phase shifts of the atmosphere and the device will cancel one another, restoring the original phase relation of the signal and eliminating the effects of atmospheric GVD.

Designing such a device, however, is not necessarily an easy task. The challenge of dispersion compensation is in designing a device that can accurately produce the desired dispersion profile. GVD in optical communications has been well studied, and many strategies exist for compensating optical dispersion, such as double-chirped mirrors, Bragg reflectors, dispersion prisms, negative dispersion fiber, and diffraction gratings being established examples. However, little work has been undertaken to develop such devices for THz frequencies, and established optical solutions are not well-suited for compensating atmospheric dispersion in THz links, from the perspective of neither design nor available materials. One reason is that optical wavelengths are much smaller than THz wavelengths, so some optical devices (such as double-chirped mirrors) become bulky at THz frequencies. Additionally, the electromagnetic properties of commonly optical materials are often different at THz frequencies, and exhibit losses that make them unsuited for use in the THz bands. Furthermore, the atmospheric group delay profile is unlike the dispersion profiles encountered in optical applications in both its shape, and more significantly in its dynamic nature. All these factors are reasons why established optical dispersion compensating technology is not appropriate for atmospheric dispersion compensation in the THz bands.

In this work, the design of a novel dispersion compensating device at THz frequencies began with a double-chirped mirror (a common negative dispersion device for optical applications) made of alternating layers of high and low index dielectrics. This was modeled in MATLAB®, using the characteristic matrices approach presented in [46]. At optical frequencies, the dielectric layers are typically made of SiO_2 and TiO_2 [47], but for THz frequencies these materials are both similar in index, so the design was modified to use air and high-resistivity float zone silicon (which may both be treated as lossless for the distances considered, and possess refractive indices of 1 and 3.417 respectively [48]). In optical applications, such mirrors have a highly reflective back section, implemented as a dielectric mirror. However, at THz frequencies, a thin sheet of metal of

several hundred microns' thickness is just as good a reflector, and is smaller and simpler to implement, so the Bragg reflector was replaced with a high-reflectivity metal sheet.

The design was further simplified by reducing the number of dielectric matching layers in front of the reflector. This resulted in the device exhibiting anomalous dispersion over a smaller bandwidth, which was acceptable as the maximum available bandwidth of the broadest THz channel is 180 GHz [30], as opposed to the design bandwidth of most double-chirped mirrors, which may be hundreds of THz [47].

More significantly, removing the matching layers meant the mirror ceased to be double chirped. The purpose of the matching layers (double-chirping) is to suppress oscillations in group delay caused by resonant trapping of the signal between the dielectric interfaces. These oscillations in group delay are considered undesirable in optical applications, and great care is taken to avoid them. However, by tuning the optical thickness of the dielectric layers, the location of these group delay ripples could be arranged so that they provided the desired anomalous dispersion over the design bandwidth. At this point, the dispersion compensating device could no longer be called a chirped mirror but was more akin to a Gires-Tournois interferometer with multiple dielectric layers - a "multiple Gires-Tournois interferometer," or MGTI [49]. Gires-Tournois interferometers are well-known optical devices comprised of a pair of partial reflectors and an (ideally) perfect reflector, separated by some distance, that produce wavelength-dependent GVD via resonant trapping of radiation between the reflectors. By arranging multiple dielectrics of differing index in front of a highly reflective metal back plate, each dielectric interface becomes a partially reflecting surface, and Gires-Tournois-interferometer-like behavior is observed, though the presence of multiple reflecting surfaces allows a more complex and tunable dependence of GVD on frequency.

The optical thickness of the dielectric layers of the MGTI were then optimized by means of a genetic algorithm. The algorithm attempts to minimize the root mean squared error between the group delay profile of the MGTI, and the group delay profile of the 'atmospheric opposite', which is generated from the atmospheric modeling process for a particular set of temperature, vapor density, and pressure.

The genetic algorithm operates by the following process. First, a small, random change is made to the thickness of one of the dielectric layers in the MGTI. The mean square error between the group delay of the modified MGTI and the goal is computed. If the change lowered the mean squared error, the change is deemed beneficial, and it is repeated until it no longer yields any improvement. Then the algorithm selects the next layer to modify and repeats the process. The algorithm loops over every dielectric layer in the stack until an adjustable number of iterations have passed without improvement, at which point the algorithm exits and return the optimized optical thickness of the dielectric layers.

Although fair matching to the target group delay profile was obtained for a single MGTI, it was found that reflecting the dispersed signal from multiple MGTIs with complementary group delay profiles in series could produce a much more precise match to the target profile. The substantial improvement in target group delay profile matching was deemed enough to justify the complexity of using a small number of reflectors in series, and the genetic algorithm was used to optimize a cohort of MGTI-type reflectors for this type of operation.

SECTION II – RESULTS

The methodology described in the previous section was used to design a dispersion compensation device and strategy capable of up compensating to 99% of the GVD theoretically possible to compensate that would be experienced by a transform-limited THz pulse propagating through 4 km of atmosphere with a water vapor density of ρ_{WV} = 10.4 g/m^3 (60% relative humidity at 20

°C). Moreover, this approach can be implemented in a monolithic device that can simply be inserted into the THz beam to correct the signal GVD, and that has an insertion loss as low as 0.07 dB (over 98% power efficient).

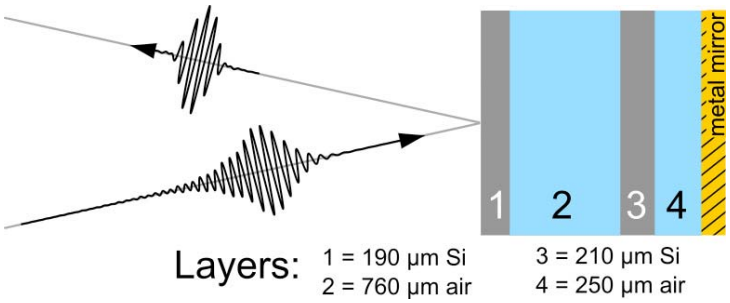

Figure 13 - Silicon-based MTGI design and concept. Temporally dispersed terahertz waves reflect from the MGTI and experience dispersion opposite that of the atmospheric channel, thus restoring their short pulsewidth.

A generalized structure for a MGTI is shown in Figure 13. While Figure 13 shows only one design, two different MGTIs (a cohort) were actually employed together to compensate the above described dispersion. Using a cohort of two MGTIs increases the effectiveness of compensation by improving the fit to the atmospheric opposite over a larger bandwidth. Each MGTI was designed with alternating layers of high-resistivity silicon (Si) and air. The layer thicknesses were optimized for a cohort of two MGTIs. The optimal layering for the first MGTI was 190 μm of silicon, 760 μm of air, 210 μm of silicon, 250 μm of air, and finally the reflector. Thickness tolerances of ± 5 μm had minor effects on the overall performance. The silicon was assumed to be lossless with a refractive index of n_{Si} =3.4174. For the second MGTI, the layering was 210 μm of silicon, 800 μm of air, 260 μm of silicon, 90 μm of air, reflector. In operation, the THz wave would reflect once from each MGTI to achieve full compensation. The cohort reflects more than 98% of incident power (0.03 dB insertion loss per MGTI per reflection) where conductor losses in the high-reflector constituted the majority loss mechanism. The cohort design also resulted in a good fit to the target group delay curve, as can be seen from Figure 14.

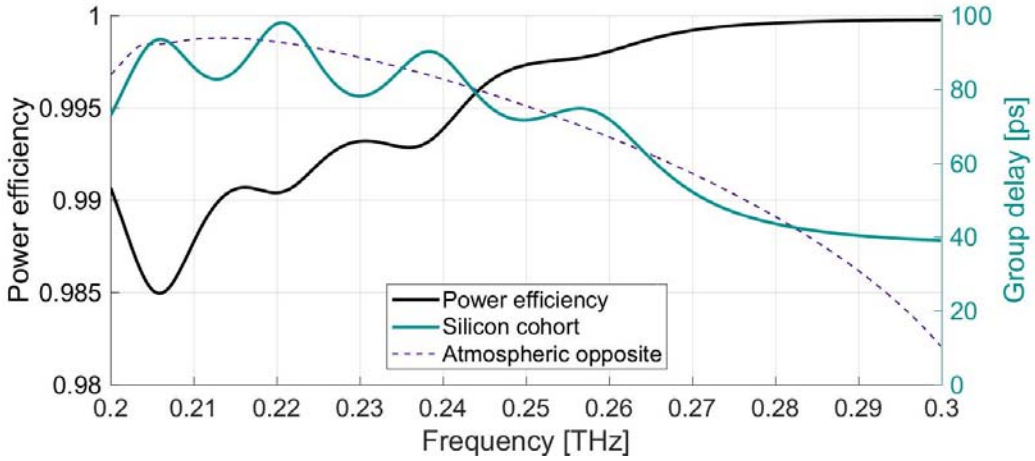

Figure 14 - Analytic performance of Si-MGTI cohort. The dashed line indicates the target group delay, the opposite of atmospheric group delay at ρ_{wv} = 10.37 g/m^3 for a 4 km propagation range. The thick black curve indicates the overall power efficiency. Plots show overall effects of one reflection from each MTGI of the cohort (two reflections total).

As a second demonstration, a cohort of MGTIs based on polytetrafluoroethylene (PTFE) layers was also designed. The first MGTI of the cohort had a layering of 480 μm of PTFE, 380 μm of air, 510 μm of PTFE, 250 μm of air, and finally the reflector. The second MGTI of the cohort had a layering of 430 μm of PTFE, 750 μm of air, 540 μm of PTFE, 290 μm of air, then the reflector. As before, the cohort was designed to compensate the dispersion produced by 4 km of propagation through the atmosphere with ρ_{WV} = 10.4 g/m^3. Note that PTFE has a lower index than silicon (a constant index n_{PTFE} = 1.42+i0.0032 was obtained using THz-TDS), which reduces the reflections at the layer boundaries, resulting in less overall dispersion. This allowed us to more precisely match the atmosphere's dispersion profile for varying water vapor densities at the expense of cumulative dispersive power.

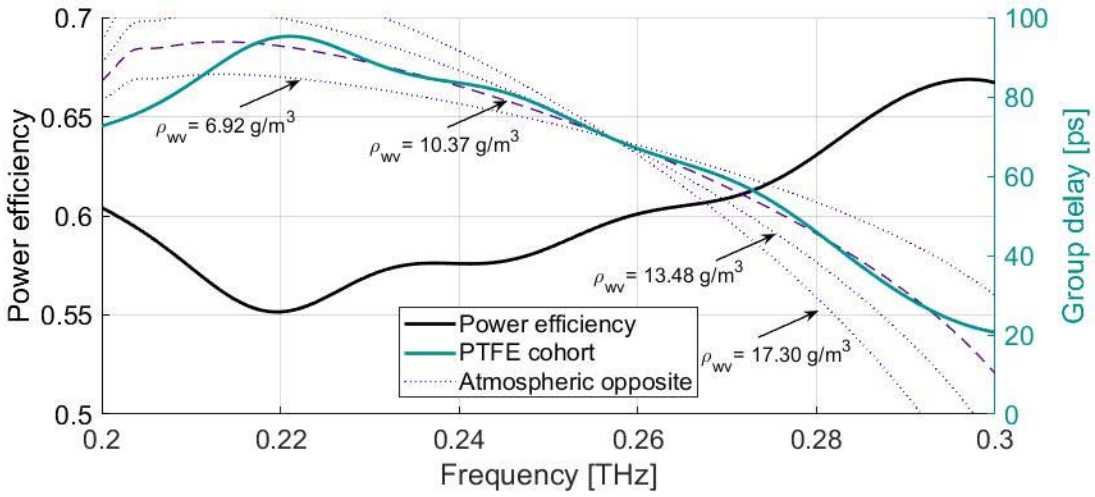

Figure 15 - Analytic performance of PTFE-MGTI cohort. The dashed line indicates the target group delay, the opposite of atmospheric group delay at ρ_{wv} = 10.37 g/m^3 for a 4 km propagation range. The dotted lines show how varying the atmospheric water vapor density for the 4 km link affects the target group delay. The increasing vapor densities given on the plot correspond to 40%, 60%, 80%, and 100% relative humidity at 20°C respectively. The thick black curve indicates the overall power efficiency. Plots show overall effects of four reflections from each MTGI of the cohort (eight reflections total).

PTFE absorptive losses are not large in the THz range, but they accumulate when waves traverse the layers of the MGTIs multiple times, leading to greater overall insertion loss than a silicon-based device. Because of this, both material and reflector losses must be accounted for. Despite this loss, the PTFE cohort is still highly effective at compensating atmospheric dispersion over shorter distances. This cohort of two MGTIs reflects more than 86% of incident power for a single pass through the cohort (0.3 dB insertion loss per MGTI per reflection). However, since its dispersive power is about 25% of the Si-based cohort, the THz beam must reflect from each PTFE-MGTI four times to compensate the target 4 km channel, which lowers the overall cohort power efficiency to 55% (minimum) or 2.6 dB insertion loss total, as shown in Figure 15. An advantage of the PTFE-cohort, apparent from Figure 15, is that it exhibits a better fit to the target group delay curve.

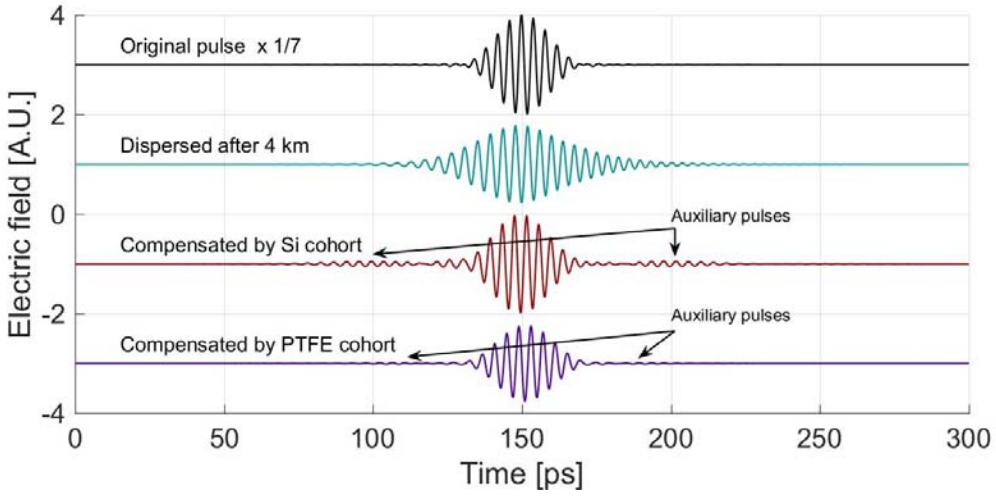

Figure 16 - Time-domain terahertz pulses before and after propagation through atmosphere and compensators. The figure shows the original pulse (black), pulse after propagation through atmosphere (blue), pulse after Si-MGTI cohort compensation (red), and pulse after PTFE-MGTI cohort (purple). All waveforms are shown to scale except the original pulse, which is scaled down in amplitude by 7 times to aid display. Auxiliary pulses are evident in compensated waveforms, as shown.

To further demonstrate the MGTI cohorts, the time-domain waveforms for THz pulses before and after compensation were calculated. Plane-wave propagation of the THz pulse through the atmosphere was assumed, at ρ_{WV} = 10.4 g/m^3, over a distance of 4 km. The initial transform-limited pulse was given a raised cosine spectrum centered at 250 GHz, with a FWHM bandwidth of 50 GHz. After propagating through the atmosphere, this pulse was dispersed to 175% of its original width by GVD and reduced in amplitude by 9.1 times due to water vapor absorption losses, as shown by the electric-field waveforms in Figure 16. For determination of the pulse width, an approximately Gaussian profile of the pulse both before and after dispersion was assumed.

This dispersed pulse was compensated by both the Si- and PTFE-based MGTI cohorts. As before, compensation was achieved by either one (Si) or four (PTFE), normal-incidence reflections off the cohort. These atmospheric conditions represent a natural transition point between the silicon and PTFE approaches. The silicon cohort cannot be used for less compensation because there can

be no less than one reflection, while the PTFE cohort is less desirable for more compensation because of accumulating losses. The analytic transfer functions of the cohorts were multiplied by the dispersed pulse spectrum in the frequency domain, then inverse Fourier transformed to obtain the time-domain output waveforms.

As shown in Figure 16, the pulse went from 175% to 105% (for both Si and PTFE) of its original width. This significant reduction in pulse width corresponds to a 66% increase in spectral efficiency, $\eta_{eff} = B/\Delta f_{ch}$ [43], where Δf_{ch} is the pulse bandwidth, and B is the bit rate, which is inversely proportional to the pulse width. These numbers do not fully describe the effectiveness of the approach. Even a perfect dispersion compensation scheme cannot fully compensate for atmospheric dispersion, because some signal bandwidth is irreversibly lost due to absorption [31]. When this is accounted for, the Si-MGTI and PTFE-MGTI cohorts both achieve >99% of the theoretically possible dispersion compensation, but the PTFE cohort is better, exhibiting excellent compensation (99.8% by calculation).

It is worth noting the missing ~1% of possible compensation for the Si cohort is manifested in the presence of "auxiliary pulses" on the compensated waveforms of Figure 16. These pulses contain very little power and are not large enough to significantly contribute to ISI. Their presence may be linked back to the frequency-dependent oscillations in the cohort's group delay around the target group delay (See Figure 14). In other words, they result from the non-zero sum of group delays of the atmosphere and the MGTIs. The auxiliary pulses can be minimized by using a lower index material (such as PTFE) to construct the MGTIs. This reduces the lifetime of resonances within the MGTI layers, thus reducing the amplitude of the group delay oscillations. For example, both the group delay oscillations (Figure 14 and Figure 15) and the auxiliary pulses (Figure 16) are much smaller for the PTFE cohort than in the Si cohort. Auxiliary pulses may also be suppressed by the addition of more layers to the MGTIs, or by the addition of more MGTIs to the cohort. However, given the exceptionally good match achieved with a small number of MGTIs

and dielectric layers, these adjustments appear unnecessary. For longer range systems, such strategies might be employed with Si-based MGTIs to obtain every advantage in both optimized dispersion compensation and low loss.

It is also worth noting that the dispersion profile of the atmosphere is a function of atmospheric water vapor density (as shown in Figure 15), thus the effectiveness of the MGTI cohort will be somewhat lessened whenever the vapor density deviates significantly from the design value. Repeating the time-domain calculations previously described for the PTFE cohort at the vapor densities shown in Figure 15 yields the following results: at $\rho_{wv} = 6.92$ g/m^3 , the input pulse is dispersed to 138% its original width, and compensated to 110% (79% of ideal). At $\rho_{wv} = 13.84$ g/m^3, the input is dispersed to 205% its original width, and compensated to 114% (93% of ideal). Finally, at $\rho_{wv} = 17.3$ g/m^3, the input is dispersed to 232% its original width, and compensated to 138% (78% of ideal). These values are for a static cohort, however, it is possible to dynamically match the changing dispersion profile of the atmosphere by altering the arrangement of the MGTIs in the cohort so that the dispersed signal is reflected from each MGTI multiple times, which increases or decreases the total amount of negative dispersion experienced by the signal as it passes through the cohort.

CHAPTER VI

DEVICE FABRICATION AND CHARACTERIZATION

SECTION I – METHODOLOGY

After generating optimized MGTI structures for various atmospheric windows, one MGTI of the PTFE-cohort (optimized for operation over the 250 GHz channel) was selected for fabrication and subsequent characterization using reflection-mode THz-TDS in order to verify that the device behaved as predicted by the mathematical models. The sample selected for fabrication was comprised of four layers of alternating dielectric – two layers of polytetrafluoroethylene (PTFE), and two of air – and an end reflector. This MGTI has an ideal structure of 480 μm of PTFE, 380 μm of air, 510 μm of PTFE, 250 μm of air, and finally an aluminum mirror. The dielectric layers were cut to 20mm diameter from commercial PTFE sheets, and were sanded by hand to the proper thicknesses because PTFE sheets of the needed thicknesses were not commercially available. Consequently, the thicknesses of the dielectric layers deviated somewhat from their target values. The PTFE layers were mounted and spaced apart using the mounting device shown in Figure 17. All layer thicknesses (both PTFE and the spacing between them) were within +/- 5 μm of the intended values except the first layer, which was made 30 μm thinner than intended. According to numerical analysis, it was predicted than these errors – apart from the 1st layer – would not significantly affect the group delay profile of the MGTI. Figure 17(b) shows the actual fabricated device alongside a schematic of its inner

structure in Figure 17(c). The MGTI diameter was made large enough (~ 12 mm) to avoid clipping the THz beam (~7 mm diameter) focused onto its surface.

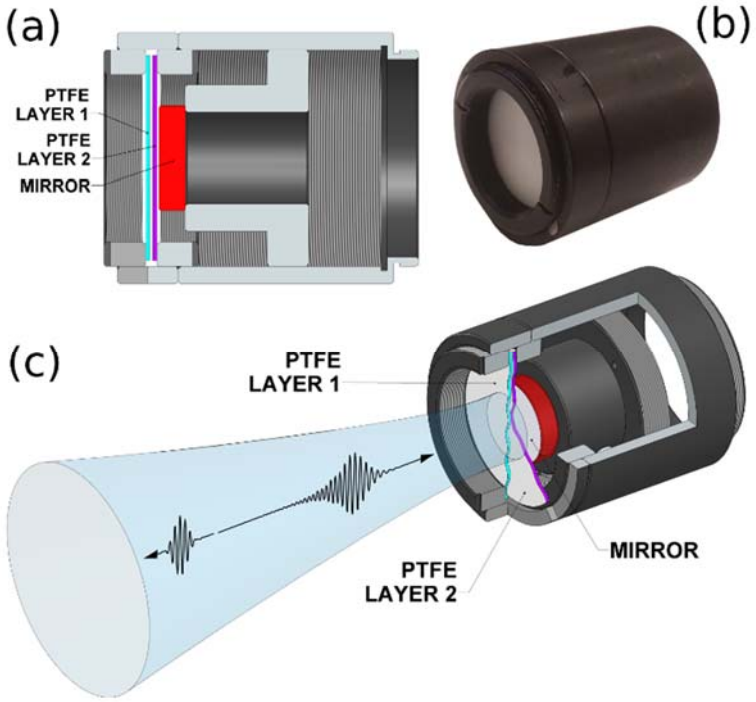

Figure 17 - A prototype terahertz dispersion compensating MGTI. (a) cross-section drawing of designed and fabricated MGTI, (b) fabricated MGTI, with PTFE first layer visible (c) scale cutaway drawing of fabricated MGTI showing internal layering. Blue tube depicts focused input/output terahertz beam.

The performance of the MGTI was measure in a reflection-mode THz-TDS setup, the schematic of which is given in Figure 18. This system permits phase-coherent measurements of both the sample and reference at normal incidence. It is modified from the standard transmission setup described in [50]. THz pulses with a signal bandwidth of 0.1 to 2 THz generated by the transmitter are collimated by an off-axis paraboloidal mirror to a 3-mm thick high-resistivity float-zone silicon beamsplitter. The thickness of the silicon beamsplitter is chosen to be large so that the initial pulse and subsequent features in the time-domain are easily separable from later echo pulses, which are caused by multiple reflections within the beamsplitter. If the beamsplitter is too thin, the time-domain features introduced by the sample will overlap with the features

introduced by the beamsplitter, significantly increasing the difficulty of extracting the sample parameters.

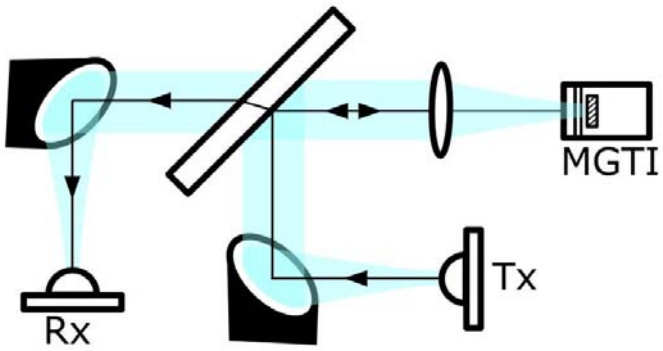

Figure 18 - Reflection-mode THz-TDS setup for normal-incidence, phase-coherent measurements. The system is confocal and produces a frequency-independent beam waist with a planar phase front at the MGTI sample. The blue shaded areas illustrate the terahertz beam profile (not to scale). Labels "Tx" and "Rx" refer to the terahertz transmitter and receiver.

After reflecting off the beamsplitter, the terahertz pulses are reflected toward and focused onto the sample at normal incidence using a polyethylene lens. At the sample, the frequency-independent beam waist diameter is ~ 7 mm. After reflecting off the sample, the broadband beam is again collimated by the polyethylene lens and then passes through the beamsplitter. It is finally focused into the THz receiver by another off-axis paraboloidal mirror. The entire system is confocal to maximize power transfer and ensure a frequency-independent beam waist diameter at the sample.

Obtaining the transfer function of the MGTI requires knowing the spectrum of the THz pulse incident on the sample. The prototype was designed so that the dielectric layers of the MGTI were separable from the reflective backing, which allowed the necessary phase reference (incident THz pulse spectrum) to be obtained reliably and simply by removing the resonant dielectric layers from the sample. This allowed the THz wave to reflect off the aluminum mirror of the sample by itself, which was mounted such that its location remained constant, whether the

dielectric layers were present or not. This establishing a fixed and reliable phase reference for proper determination of the sample transfer function.

SECTION II – RESULTS

The results obtained through experimental measurements validated the behavior of the device predicted by the analytic models. The measured and predicted time-domain traces are compared in Figure 19, in which it is evident that the predicted and measured waveforms are very similar. This shows that the model of the MGTI is a very good predictor of the physical MGTI's behavior over the entire measured frequency range (~0.1-2.5 THz), both in phase and amplitude. A notable discrepancy between the measured and predicted waveforms is found at the very first (leftmost) feature on the plot. This feature is the reflection off the first PTFE layer of the MGTI, and its time misalignment and reduction in amplitude reflects the fact that this layer was fabricated thinner than intended.

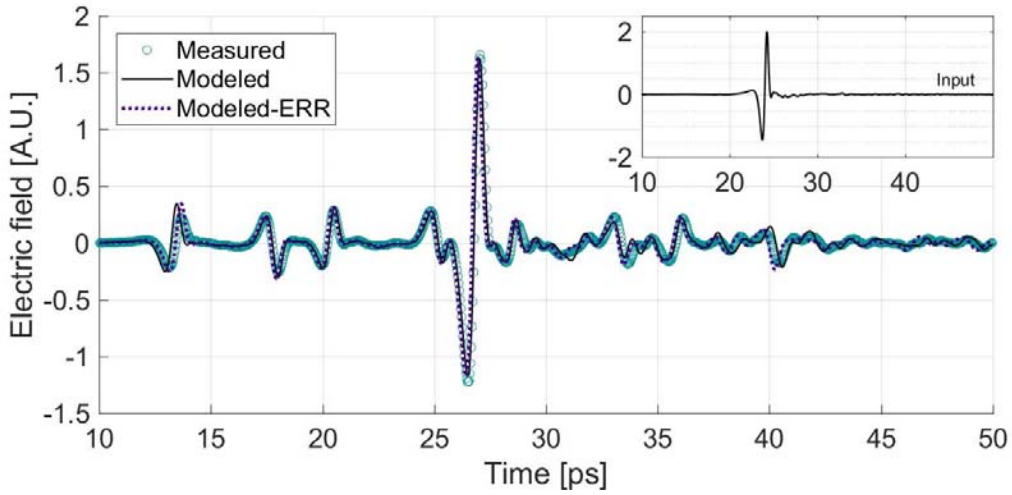

Figure 19 - Measured and predicted time-domain waveforms for THz pulses reflected from the PTFE MGTI shown in Figure 17. The inset shows the measured reference pulse, obtained by removing the two PTFE layers in front of the reflector. The units of the inset are the same as those of the main plot.

The measured data was also analyzed in the frequency domain to extract the group delay of the sample and compare it to model predictions, as shown in Figure 20. Again, there is good

agreement between the modeled and measured values, which confirms both the analytical calculations and the validity of the GVD compensation approach. Note that these curves represent the effect of only one reflection from one MGTI of the cohort, hence the graphs of Figure 20 and Figure 15 are different.

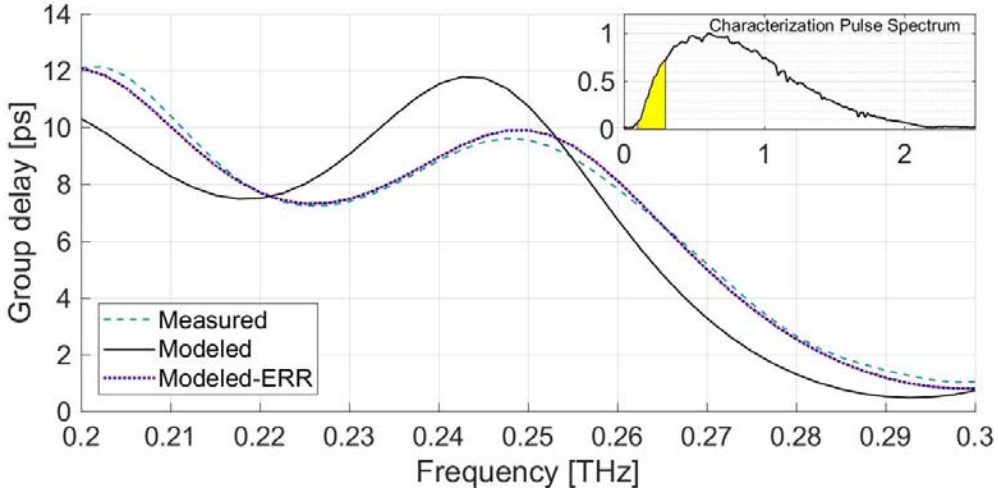

Figure 20 - Measured and predicted group delay for THz waves reflected from the PTFE MGTI shown in Figure 17. The inset shows the spectrum of the THz pulse used to characterize the sample (see inset of Figure 19). The units of the inset axes are frequency (THz) along the x-axis, and normalized spectrum amplitude on the y-axis. The shaded area is the 200-300 GHz band over which the sample was characterized.

Discrepancies between measured and predicted results arise primarily because the fabrication techniques could not exactly produce the desired layer thicknesses nor uniformity. Specifically, the thickness of the first PTFE layer was measured to be 450 μm, or 30 μm thinner than intended. When the model is modified to account for this error, the predicted and measured group delay profiles are in even closer agreement, as shown by the trace labeled "Modeled-ERR" in both Figure 19 and Figure 20. The experimental results confirm that the analytic calculations are accurate, and that such devices are readily designed and fabricated.

SECTION III - DISCUSSION

Since the THz wireless channel would generally be dynamic, both in terms of atmospheric properties (weather) and signal range, it is important to address the adaptability of the approach to changing channel conditions. The dispersion of an MGTI cohort can be dynamically adapted most easily by altering the number of times the THz beam is reflected from it. By mechanically adjusting the angle and position of the individual cohort members, the dispersed signal can be made to undergo more or fewer reflections from each MGTI as desired, which corresponds to a discrete increase or decrease in the level of dispersion achieved. By using a low-index dielectric MGTI in the cohort, the resolution of these discrete changes can be very fine, making it possible to compensate effectively a continuous range of changing atmospheric conditions and ranges. Even though changing the number of reflections would be a slow tuning procedure, it is more than sufficient for this application because channel conditions also change quite slowly.

Altering the physical geometry of the signal path to either add or reduce the number of reflections will also mean changing the angle at which the wave is incident on each MGTI. However, the complex reflection coefficient of a stratified dielectric is a function of incidence angle and polarization [46]. Thus, there is a limit to how obliquely the signal may strike each MGTI before the cohort will no longer adequately compensate the atmospheric dispersion. Calculations show that the silicon cohort described previously will still achieve 90% or greater of the possible dispersion compensation as long as the incidence angle for all MGTIs is less than 15° off normal in either direction, for both *s* and *p* polarizations. This is sufficiently flexible for the mechanical tuning techniques described above, and it also illustrates the excellent robustness of the technique to practical alignment errors. The dependence of compensated pulse shape on incidence angle for the Si cohort is shown in Figure 21 for a *p*-polarized (worst case) incident pulse.

It is important to note that the effectiveness of this dispersion-compensating approach does not depend on the form or modulation of the incident THz signal. Though the figures and analyses show the dispersion and subsequent compensation of transform-limited pulses (as would be used in impulse radio), continuous-wave modulation schemes such as quadrature amplitude modulation and frequency-shift keying will suffer dispersion in like manner, and will be compensated with the same effectiveness. This is because GVD is a function of channel properties only. Regardless of modulation, any THz signal with a given bandwidth, having suffered dispersion in the atmosphere, will be compensated by interacting with a device exhibiting a group velocity dispersion opposite the atmosphere over that same bandwidth.

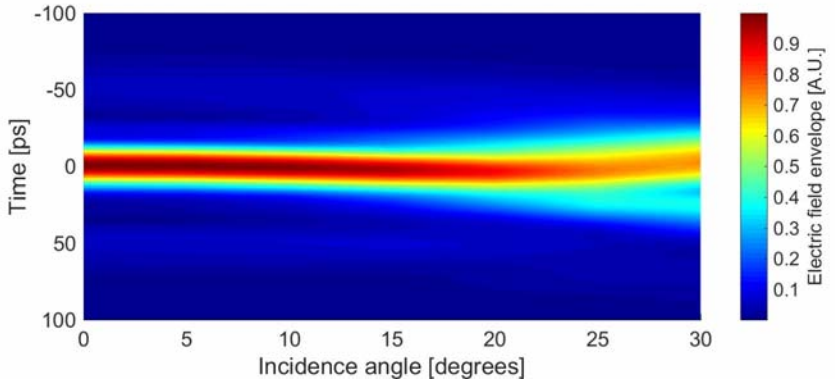

Figure 21 - Time-domain compensated THz pulse evolution as a function of incidence angle on the Si-MGTI cohort, assuming p-polarization. Unlike Figure 16, the normalized envelope of the electric field is shown for clarity. The pulse begins to noticeably disperse in time when the obliquity angle exceeds 15°.

CHAPTER VII

CONCLUSION

Databases of molecular resonances, in conjunction with MRT, allows the transfer function of the atmosphere the be modeled with high fidelity over the THz communication bands. This allows highly accurate predictions of the time-domain distortions imposed on a modulated THz digital data stream by atmospheric attenuation and dispersion.

By performing an end-to-end THz digital communication simulation of a QPSK link with the atmospheric effects incorporated, it was found that GVD is non-negligible in wideband THz link design, and limits both transmission distance and SER in conjunction with atmospheric attenuation. At lower bandwidths (below 20 Gbit/s), absorption was found to be the dominant mechanism limiting link distance. This is no surprise, and matches the prevailing assumption in the literature. However, for increasingly high bandwidths, the simulations reveal that dispersion, and not atmospheric absorption, is the factor that limits the maximum distance of the link. This agrees with the observations of Mandehgar *et al*, [30] but the work presented here provides far greater insight in the relationship between SER, bit rate, link distance, and SNR for high-bandwidth, long distance THz links than any other study published to date.

A significant finding of this work is that high bandwidth links are dispersion-limited, and that theoretical predictions of SER based only on SNR are not valid for high-bandwidth, long distance

THz links. In the literature, it is generally assumed that increasing the power of the THz transmitter corresponds to increasing the distance over which data may be reliably transmitted. This may be true in some cases, but only up to a certain point. Once the dispersion limit is reached, GVD becomes the dominant factor is determining link performance, and increasing the SNR no longer yields any improvement in SER. This means that no matter how powerful a transmitter is developed, the maximum transmission range of a THz link cannot exceed a certain, finite distance. This dispersion limit on maximum range decreases rapidly with both increasing bandwidth and increasing vapor density.

An important, related finding was that the presence of noise makes the negative effects of dispersion in a THz link occur at distances under the dispersion limit, and this effect is most noticeable in links that possess a high dispersion limit (that is, lower bandwidth links). The implication is that dispersion cannot be neglected even below the dispersion limit. Operating below the dispersion limit does not guarantee freedom from GVD-induced ISI, but only that increasing the SNR will improve the SER of the link.

This work also demonstrated that structurally simple and inexpensive MGTIs can be readily designed to compensate atmospheric dispersion, thus removing the dispersion limit. Assembling these MGTIs into a cohort allows for moderate tuning to better match changing atmospheric conditions, and allows increasingly precise matches to the atmospheric group delay profile to be made. MGTI cohorts are an effective method of compensating atmospheric dispersion in long-distance THz wireless links to thereby maximize data transmission rates to their fundamental limit. To the knowledge of the author, these devices are the first of their kind in the THz regime, and this work represents an important step toward the implementation of point-to-point and point-to-mobile THz wireless links. Furthermore, compensating devices such as the ones presented here are highly effective in terms of both complete dispersion management and low loss, inexpensive to fabricate, and moderately tolerant to manufacturing errors. Though not discussed in this paper,

they may also be easily optimized for oblique incidence, which allows for flexibility in how such devices are physically incorporated into THz communication systems.

By revealing that dispersion places a fundamental limitation on the range of high-bandwidth THz communication links, and by demonstrating that dispersion may affect link performance well below the dispersion limit, this thesis has established GVD as a factor that must be included in the design and analysis of future wideband THz communication links. By presenting a novel and highly effective strategy for compensating GVD in THz wireless communication links, this work has also laid a foundation for the development of future THz dispersion management technologies.

REFERENCES

[1] J. Wells, "Faster than fiber: The future of multi-G/s wireless.," *IEEE Microwave Magazine,* vol. 10, no. 3, p. 104–112, 2009.

[2] S. Cherry, "Edholm's law of bandwidth.," *IEEE Spectrum,* vol. 41, no. 7, pp. 58-60, 2004.

[3] H.-J. Song and T. Nagatsuma, "Present and Future of Terahertz Communications," *IEEE Transactions on Terahertz Science and Technology,* vol. 1, no. 1, pp. 256-263, 2011.

[4] A. V. Dastjerdi and R. Buyya, "Fog Computing: Helping the Internet of Things Realize Its Potential," *Computer,* vol. 49, no. 8, pp. 112-116, 2016.

[5] Y. Qi *et al.*, "Quantifying data rate and bandwidth requirements for immersive 5G experience," in *2016 IEEE International Conference on Communications Workshops (ICC)*, Kuala Lumpur, 2016.

[6] Cisco, "Global mobile data traffic forecast update, 2018-2023," 9 March 2020. [Online]. Available: https://www.cisco.com/c/en/us/solutions/collateral/executive-perspectives/annual-internet-report/white-paper-c11-741490.html. [Accessed 13 April 2020].

[7] J. Ma, R. Shrestha, L. Moeller and D. M. Mittleman, "Invited Article: Channel performance for indoor and outdoor terahertz wireless links.," *APL Photonics,* vol. 3, no. 5, 2018.

[8] Y. Yang, M. Mandehgar and D. Grischkowsky, "THz-TDS Characterization of the Digital Communication Channels of the Atmosphere and the Enabled Applications," *Journal of Infrared, Millimeter, and Terahertz Waves,* vol. 36, pp. 97-129, 2015.

[9] Z. Chen and et al, "A survey on terahertz communications," *China Communications,* vol. 16, no. 2, pp. 1-35, 2019.

[10] G. Ducournau *et al.*, "Ultrawide-Bandwidth Single-Channel 0.4-THz Wireless Link Combining Broadband Quasi-Optic Photomixer and Coherent Detection," *IEEE Transactions on Terahertz Science and Technology,* vol. 4, no. 3, pp. 328-337, 2014.

[11] T. Kleine-Ostmann and T. Nagatsuma, "A Review on Terahertz Communications Research," *Journal of Infrared, Millimeter, and Terahertz Waves,* vol. 32, p. 143–171, 2011.

[12] Q. Wu *et al.*, "A 21 km 5 Gbps real time wireless communication system at 0.14 THz," in *2017 42nd International Conference on Infrared, Millimeter, and Terahertz Waves (IRMMW-THz)*, Cancun, 2017.

[13] X. Li *et al.*, "Fiber-Wireless-Fiber Link for 100-Gb/s PDM-QPSK Signal Transmission at W-Band," *IEEE Photonics Technology Letters,* vol. 26, no. 16, pp. 1825-1828, 2014.

[14] M. Mandehgar, Y. Yang and D. Grischkowsky, "Atmosphere characterization for simulation of the two optimal wireless terahertz digital communication links," *Optics Letters,* vol. 38, pp. 3437-3440, 2013.

[15] G. A. Siles, J. M. Riera and P. Garcia-del-Pino, "Atmospheric Attenuation in Wireless Communication Systems at Millimeter and THz Frequencies [Wireless Corner]," *IEEE Antennas and Propagation Magazine,* vol. 57, no. 1, pp. 48-61, 2015.

[16] D. M. Slocum *et al.*, "Terahertz atmospheric attenuation and continuum effects," in *Proceedings of SPIE volume 8716, Terahertz Physics, Devices, and Systems VII: Advanced Applications in Industry and Defense*, Baltimore, Maryland, 2013.

[17] T. Yuan *et al.*, "Terahertz time-domain spectroscopy of atmosphere with different humidity," in *Proceedings of SPIE volume 5070, Terahertz for Military and Security Applications*, Orlando, Florida, 2003.

[18] Y. Yang, A. Shutler and D. Grischkowsky, "Measurement of the transmission of the atmosphere from 0.2 to 2 THz," *Optics Express,* vol. 19, no. 9, pp. 8830-8838, 2011.

[19] R. J. Hill, "Dispersion by atmospheric water vapor at frequencies less than 1 THz," *IEEE Transactions on Antennas and Propagation,* vol. 36, no. 3, pp. 423-430, 1988.

[20] Y. Yang, M. Mandehgar and D. Grischkowsky, "Understanding THz Pulse Propagation in the Atmosphere," *IEEE Transactions on Terahertz Science and Technology,* vol. 2, no. 4, pp. 406-415, 2012.

[21] T. Schneider *et al.*, "Link Budget Analysis for Terahertz Fixed Wireless Links," *IEEE Transactions on Terahertz Science and Technology,* vol. 2, no. 2, pp. 250-256, 2012.

[22] J. H. Van Vleck and V. F. Weisskoph, "On the Shape of Collision-Broadened Lines," *Review of Modern Physics,* vol. 17, no. 2-3, pp. 227-236, 1945.

[23] D. Grischkowsky, Y. Yang and M. Mandehgar, "Zero-frequency refractivity of water vapor, comparison of Debye and van-Vleck Weisskopf theory," *Optics Express,* vol. 21, no. 16, pp. 18899-18908, 2013.

[24] H. Pickett *et al.*, "Submillimeter, millimeter, and microwave spectral line catalogue, revision 3," Jet Propulsion Lab, California Instute of Technology, Pasadena, California, 1992.

[25] L. Rothman *et al.*, "The HITRAN 2008 molecular spectroscopic database," *Journal of Quantitative Spectroscopy and Radiative Transfer,* vol. 110, no. 9-10, pp. 533-572, 2009.

[26] H. Harde, R. Cheville and D. Grischkowsky, "Terahertz Studies of Collision-Broadened Rotational Lines," *The Journal of Physical Chemistry A,* vol. 101, no. 20, pp. 3646-3660, 1997.

[27] Y. Yang, M. Mandehgar and D. Grischkowsky, "Determination of the water vapor continuum absorption by THz-TDS and Molecular Response Theory," *Optics Express,* vol. 22, no. 4, pp. 4388-4403, 2014.

[28] M. van Exter, C. Fattinger and D. Grischkowsky, "Terahertz time-domain spectroscopy of water vapor," *Optics Letters,* vol. 14, no. 20, pp. 1128-1130, 1989.

[29] J. O'Hara and D. Grischowkowsky, "Comment on the Veracity of the ITU-R Recommendation for Atmospheric Attenuation at Terahertz Frequencies," *IEEE Transactions on Terahertz Science and Technology,* vol. 8, no. 3, pp. 372-375, 2018.

[30] M. Mandehgar, Y. Yang and D. Grischkowsky, "Experimental confirmation and physical understanding of ultra-high bit rate impulse radio in the THz digital communication channels of the atmosphere," *Journal of Optics,* vol. 16, no. 9, 2014.

[31] M. Mandehgar and D. Grischkowsky, "Understanding Dispersion Compensation of the THz Communication Channels in the Atmosphere," *IEEE Photonics Technology Letters,* vol. 27, no. 22, pp. 2387-2390, 2015.

[32] K. Strecker, S. Ekin and J. O'Hara, "Compensating Atmospheric Channel Dispersion for Terahertz Wireless Communication," *Scientific Reports,* vol. 10, no. 1, pp. 1-8, 2020.

[33] T. Nagatsuma, G. Ducournau and C. Renaud, "Advances in terahertz communications accelerated by photonics," *Nature Photonics,* vol. 10, p. 371–379, 2016.

[34] C. Wang, C. Lin, Q. Chen, X. Deng and J. Zhang, "0.14THz high speed data communication over 1.5 kilometers," in *2012 37th International Conference on Infrared, Millimeter, and Terahertz Waves*, Wollongong, NSW, 2012.

[35] A. Hirata *et al.*, "5.8-km 10-Gbps data transmission over a 120-GHz-band wireless link," in *2010 IEEE International Conference on Wireless Information Technology and Systems*, Honolulu, 2010.

[36] A. Hirata *et al.*, "120-GHz-Band Wireless Link Technologies for Outdoor 10-Gbit/s Data Transmission," *IEEE Transactions on Microwave Theory and Techniques,* vol. 60, no. 3, pp. 881-895, 2012.

[37] I. Kallfass, I. Boes, T. Messinger *et al.*, "64 Gbit/s Transmission over 850 m Fixed Wireless Link at 240 GHz Carrier Frequency," *Journal of Infrared, Millimeter, and Terahertz Waves,* vol. 36, pp. 221-233, 2015.

[38] Q. Wu *et al.*, "A 21 km 5 Gbps real time wireless communication system at 0.14 THz," in *2017 42nd International Conference on Infrared, Millimeter, and Terahertz Waves (IRMMW-THz)*, Cancun, 2017.

[39] K. Naganuma, K. Mogi and H. Yamada, "Group-delay measurement using the Fourier transform of an interferometric cross correlation generated by white light," *Optics Letters,* vol. 15, no. 7, pp. 393-395, 1990.

[40] T. Amotchkina, A. Tikhonravov, M. Trubetskov, D. Grupe, A. Apolonski and V. Pervak2, "Measurement of group delay of dispersive mirrors with white-light interferometer," *Applied optics,* vol. 48, no. 5, pp. 949-956, 2009.

[41] S. Wilson, Digital Modulation and Coding, Upper Saddle River, New Jersey: Prentice-Hall, Inc., 1996.

[42] H. Nyquist, "Certain Topics in Telegraph Transmission Theory," *Transactions of the American Institute of Electrical Engineers,* vol. 47, no. 2, pp. 617-644, 1928.

[43] G. Agrawal, Fiber-Optic Communication Systems, 4th edition, Wiley-Blackwell, 2010.

[44] R. Boyd, Nonlinear Optics (3rd edition), Burlington, Massachusetts: Academic Press, 2008.

[45] J. Barry and E. Lee, Digital Communication (3rd ed.), Norwell, Massachusetts: Kluwer Academic Publishers, 2004.

[46] M. Born and E. Wolf, Principles of Optics: Electromagnetic Theory of Propagation, Interference and Diffraction of Light (7th edition), Cambridge University Press, 2002.

[47] N. Matuschek, F. Kartner and U. Keller, "Theory of double-chirped mirrors," *IEEE Journal of Selected Topics in Quantum Electronics,* vol. 4, no. 2, pp. 197-208, 1998.

[48] J. Dai, J. Zhang, W. Zhang and D. Grischkowsky, "Terahertz time-domain spectroscopy characterization of the far-infrared absorption and index of refraction of high-resistivity, float-zone silicon," *Journal of the Optical Society of America B,* vol. 21, no. 7, pp. 1379-1386, 2004.

[49] B. Golubovic, R. Austin, M. Steiner-Shepard, M. Reed, S. Diddams, D. Jones and A. Van Engen, "Double Gires–Tournois interferometer negative-dispersion mirrors for use in tunable mode-locked lasers," *Optics Letters,* vol. 25, no. 4, pp. 275-277, 2000.

[50] M. Van Exter and D. Grischkowsky, "Characterization of an optoelectronic terahertz beam system," *IEEE Transactions on Microwave Theory and Techniques,* vol. 38, no. 11, pp. 1684-1691, 1990.

VITA

Karl Louthan Strecker

Candidate for the Degree of

Master of Science

Thesis: GROUP VELOCITY DISPERSION MANAGEMENT IN TERAHERTZ WIRELESS COMMUNICATION CHANNELS

Major Field: Electrical Engineering

Biographical:

Education:

Completed the requirements for the Master of Science in Electrical Engineering at Oklahoma State University, Stillwater, Oklahoma in May, 2020.

Completed the requirements for the Bachelor of Science in Electrical Engineering at Oklahoma State University, Stillwater, Oklahoma, 2018.

Experience:

Graduate Research Assistant, Ultrafast Optoelectronics Laboratory, Oklahoma State University (2018-Present)

Measurement Development Assistant, REFTAS Laboratory, Oklahoma State University (2017-2018).

Publications:

K. Strecker, S. Ekin and J. O'Hara, "Compensating Atmospheric Channel Dispersion for Terahertz Wireless Communication," *Scientific Reports,* vol. 10, no. 1, pp. 1-8, 2020.

Awards:

National Science Foundation Graduate Research Fellowship (*NSF GRFP*), 2020.